MODELING ASPECTS AND COMPUTATIONAL METHODS FOR SOME RECENT PROBLEMS OF TOMOGRAPHIC IMAGING

A Dissertation

by

MORITZ ALLMARAS

Submitted to the Office of Graduate Studies of
Texas A&M University
in partial fulfillment of the requirements for the degree of

DOCTOR OF PHILOSOPHY

December 2011

Major Subject: Mathematics

MODELING ASPECTS AND COMPUTATIONAL METHODS FOR SOME RECENT PROBLEMS OF TOMOGRAPHIC IMAGING

A Dissertation

by

MORITZ ALLMARAS

Submitted to the Office of Graduate Studies of
Texas A&M University
in partial fulfillment of the requirements for the degree of

DOCTOR OF PHILOSOPHY

Approved by:

Co-Chairs of Committee,	Wolfgang Bangerth
	Peter Kuchment
Committee Members,	William Rundell
	Brian E. Applegate
Head of Department,	Emil Straube

December 2011

Major Subject: Mathematics

ABSTRACT

Modeling Aspects and Computational Methods for Some
Recent Problems of Tomographic Imaging. (December 2011)
Moritz Allmaras, Diplom, Technical University of Munich;
M.S., Georgia Institute of Technology
Co–Chairs of Advisory Committee: Dr. Wolfgang Bangerth
Dr. Peter Kuchment

In this dissertation, two recent problems from tomographic imaging are studied, and results from numerical simulations with synthetic data are presented.

The first part deals with ultrasound modulated optical tomography, a method for imaging interior optical properties of partially translucent media that combines optical contrast with ultrasound resolution. The primary application is the optical imaging of soft tissue, for which scattering and absorption rates contain important functional and structural information about the physiological state of tissue cells. We developed a mathematical model based on the diffusion approximation for photon propagation in highly scattering media. Simple reconstruction schemes for recovering optical absorption rates from boundary measurements with focused ultrasound are presented. We show numerical reconstructions from synthetic data generated for mathematical absorption phantoms. The results indicate that high resolution imaging with quantitatively correct values of absorption is possible. Synthetic focusing techniques are suggested that allow reconstruction from measurements with certain types of non-focused ultrasound signals. A preliminary stability analysis for a lin-

earized model is given that provides an initial explanation for the observed stability of reconstruction.

In the second part, backprojection schemes are proposed for the detection of small amounts of highly enriched nuclear material inside 3D volumes. These schemes rely on the geometrically singular structure that small radioactive sources represent, compared to natural background radiation. The details of the detection problem are explained, and two types of measurements, collimated and Compton-type measurements, are discussed. Computationally, we implemented backprojection by counting the number of particle trajectories intersecting each voxel of a regular rectangular grid covering the domain of detection. For collimated measurements, we derived confidence estimates indicating when voxel trajectory counts are deviating significantly from what is expected from background radiation. Monte Carlo simulations of random background radiation confirm the estimated confidence values. Numerical results for backprojection applied to synthetic measurements are shown that indicate that small sources can be detected for signal-to-noise ratios as low as 0.1%.

ACKNOWLEDGMENTS

First and foremost, I would like to express my deepest gratitude to Prof. Wolfgang Bangerth. From the very start of my program at Texas A&M University, his support and encouragement have been a tremendous help. It was only through his advice that I was able to overcome the numerous minor and major obstacles I encountered on the way to the completion of this dissertation.

Furthermore, I am indebted to Prof. Peter Kuchment, whose tremendous mathematical intuition has frequently proven invaluable in guiding my research in the right direction. He encouraged and supported my participation in several conferences and workshops, from which my mathematical understanding has greatly benefited.

I thank Professors William Rundell and Brian E. Applegate for kindly serving on my committee, and Prof. Jean Ragusa for his interest in my research. My work on the second part of this dissertation has greatly benefited from numerous discussions with Dr. Yulia Hristova, for which I am very grateful.

I am thankful to the faculty and staff at the Mathematics Department of Texas A&M University for providing an effective and enjoyable learning environment. In particular, I would like to thank Ms. Monique Stewart for helping me stay on top of deadlines and fight red tape on countless occasions.

I gratefully acknowledge funding I received from NSF under grant DMS-0604778 and KAUST under Award No. KUS-C1-016-04. I am thankful to KAUST, IAMCS of Texas A&M University, IMA, MSRI and AMS for providing travel funding and access to several highly interesting conferences and workshops.

Finally, this dissertation could not have come into existence without the unconditional support from my family. I owe everything to them.

TABLE OF CONTENTS

Page

CHAPTER Page

CHAPTER Page

LIST OF FIGURES

FIGURE Page

FIGURE Page

FIGURE Page

CHAPTER I

INTRODUCTION

The term *tomography* in its original meaning refers to imaging by slices. In early tomographic methods, X-ray images of the human body were collected slice by slice. Today, tomography subsumes a variety of techniques that aim at imaging the internal structure of objects by measuring their interaction with certain types of excitations like electromagnetic waves (X-rays, gamma radiation, optical light), elastic waves (ultrasound, seismic waves) or particle radiation (neutrons, electrons). The measured data does not by itself constitute an image, but rather it needs to be processed by a reconstruction algorithm to create meaningful images. The reconstruction procedure is usually based on a physical model of the interaction between matter and the excitation, as well as the measuring process. This distinguishes *computed tomography* from *direct imaging* techniques, where the measured data itself constitutes the image. Common to all tomographic methods is their non-invasive nature: The excitation is generated and data is collected only outside the object of interest, and information about the interior structure is recovered without requiring physical access to the object's inside.

Common applications of tomography are found in medical imaging, geophysical imaging, oceanography and industrial testing. In geophysics, seismic tomography is used to explore the underground structure and locate boundaries between layers of different materials like rock, soil or sand. Major applications include discovery

---

This dissertation follows the style of the SIAM Journal on Applied Mathematics.

and survey of oil reservoirs and underground aquifiers, as well as learning about the interior structure of the earth on a global scale. In oceanography, topography of the seafloor and temperature distribution in the oceans are studied using sonography. Industrial testing applications include the detection of cracks and faults in components with high reliability requirements like airplane wings, propellor blades or engine cylinders.

The use of tomographic techniques for medical diagnostics was greatly advanced with the invention of X-ray computed tomography (CT) by Cormack and Hounsfield in the early 1970s. Shortly thereafter, CT was complemented by magnetic resonance imaging (MRI), single-photon emission computed tomography (SPECT) and positron emission tomography (PET) (see [21, 24] for an overview), all of which are widely used by today's medical practitioners. These imaging modalities differ in setup, type of excitation used, and the physical quantities they are sensitive to. While CT reconstructs internal X-ray attenuation, MRI images are related to density of hydrogen atoms, and SPECT and PET images show the distribution of certain radioactive isotopes. Likewise, the multitude of tomographic imaging methods available for medical diagnostics can be explained by the need to visualize different aspects of the body's interior in order to diagnose different types of diseases.

A particular material property that has been of interest for research during recent years are the optical characteristics of biological tissue that is transmissive or translucent to optical light. Absorption and scattering rates, and, in some applications, fluorescent emission in the optical spectrum, carry important information about the physiological and structural state of tissue (see [14] for an overview). It

has been found that blood oxigenization, increased hemoglobin concentration and hypermetabolism, all of which can be linked to tumor growth, are characterized by an increase in optical absorption and scattering rates. Hence, the imaging of optical tissue properties has the prospect of allowing early diagnosis of cancer in tissue.

The first part of this text deals with the mathematics of a relatively new method for optical imaging of tissue, the so-called *ultrasound modulated optical tomography*. In this imaging modality, the high optical contrast for cancer detection is combined with the high resolution of ultrasound imaging. While many experimental studies have been carried out and physical models for this technique have been developed over the last decade, a concise mathematical model linking the measurements to the optical properties of the medium still seems to be missing. Such a model, together with computational reconstruction schemes, numerical examples and initial theoretical analysis is the topic of the first part of this dissertation. The discussion closely follows the findings reported in [4].

In the second part, a problem arising in homeland security is treated using common techniques from tomographic reconstruction. The goal is to detect the presence of small sources of highly enriched nuclear material amongst a strong background of random noise. Some evidence is presented that backprojection, a well-known ingredient of many reconstruction schemes for computed tomography, can be a useful tool in detecting sources with a very low ballistic signal-to-noise ratio (SNR), assuming that sources are sufficiently small and the background is random. Such problems with very low SNR do not normally lend themselves to tomographic imaging methods, since strong random noise can easily deteriorate reconstructions to a level where

they are no longer useful. However, for detection it is not required to reconstruct quantitatively correct images, and it will be shown that under these circumstances backprojection can yield valuable results. The discussion is based on findings in a 2D setting presented in [5, 19], and extends these results to the practically important case of detection inside 3D volumes.

CHAPTER II

RECONSTRUCTIONS IN ULTRASOUND MODULATED OPTICAL TOMOGRAPHY

2.1. Introduction

In this section, we first consider the properties and setup of optical tomography (OT) as a biomedical imaging modality. A fundamental issue of optical tomography is the limited resolution, and modulation by focused ultrasound is introduced as one possible way of overcoming this limitation. We discuss the idea and setup of ultrasound modulated optical tomography, and outline the past developments in the field. A brief discussion of the idea behind the mathematical model used in this text follows, and the section concludes with an overview of the different aspects covered in this text.

2.1.1. Optical tomography

In optical tomography, the target quantity for imaging are the optical properties of materials that are permeable to photons in the optical spectrum. Primary application is the imaging of soft tissue like the human breast and brain. In OT, objects are irradiated by optical light, usually delivered by a laser beam or through fiber optics. Typically, light in the near-infrared (NIR) spectrum with wavelengths around 700 nm is used, which can penetrate several centimeters deep into soft tissue. Sensors are placed around the object to detect scattered photons in reflection or transmission configuration. Photomultipliers, CCD cameras or interferometers are common

sensors in OT. Different variations of the OT modality exist in which optical excitations are pulsed, amplitude-modulated or of direct-current type. If coherent light is used for excitation, interference of scattered photons causes interference patterns, so-called *speckle patterns*, on the object's surface, whose characteristics are recorded by some OT variants. The sensor signals are then fed to a computer reconstruction algorithm that recovers the distribution of internal optical properties of the medium. The general setup of the OT measurement process is depicted in Figure 2.1. See [62] for an overview of different types of OT modalities.

Absorption and scattering rates of soft tissue are related to blood oxigenization, hemoglobin and melanin concentration. Elevated levels result form increased angiogenesis and hypermetabolism, both of which are indicative of tumor growth. Hence, OT images have high contrast for the detection of early stages of cancer in soft tissue. Optical light as non-ionizing electromagnetic radiation is harmless to the human organism, unlike X-ray radiation used in CT or gamma rays in PET or SPECT. Sensors and sources for optical light are highly developed, inexpensive and widely available. This makes OT imaging relatively inexpensive in comparison to other tomographic imaging methods.

Most types of optically translucent tissue are also *turbid*, i.e. highly scattering in the optical spectrum. Individual photons undergo mutiple scattering events before they can be detected by sensors. Typical scattering rates in soft tissue are on the order of one scattering event per millimeter of path length. Consequently, information about initial photon directions is rapidly lost as photons propagate through the tissue. The rapid diffusion of photons implies that reconstruction from boundary

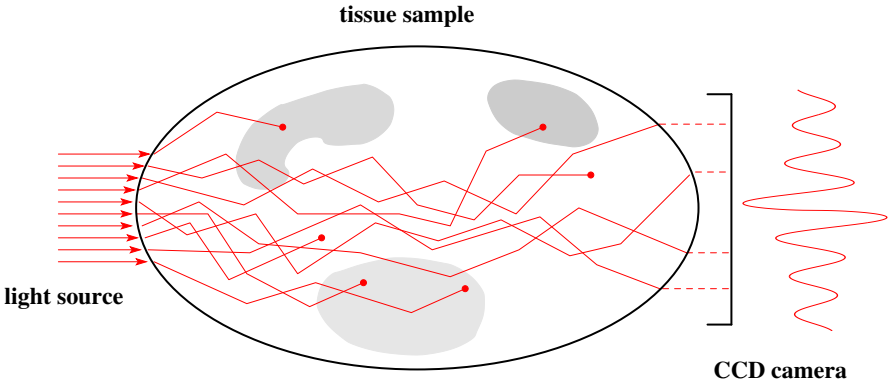

Fig. 2.1. Experimental setup in optical tomography.

measurements is severely ill-posed, rendering sharp imaging of interior optical properties all but impossible. Hence, existing optical tomography devices are restricted to thin objects (e.g. skin) or low resolution [7].

2.1.2. Ultrasound modulated optical tomography

In order to reduce the ill-posedness of the original optical tomography procedure, interactions of the optical signal with other types of excitations can be studied. The idea of such *hybrid imaging methods* is to combine the beneficial properties of two physically different excitations. See [62] for a practical discussion of hybrid optical imaging methods. For example, in photoacoustic tomography, a short light pulse initiates rapid thermal expansion of the cells inside a tissue sample, which generates an elastic wave that can be detected by ultrasound sensors placed along the surface of the object. In this imaging modality, the optical signal acts as an excitation for an acoustic wave, hence combining the high contrast of optical imaging for detection

of cancer cells with the high resolution of ultrasound imaging.

The hybrid imaging method that is the subject of this text to some extent reverses the principle of photoacoustic tomography: In ultrasound modulated optical tomography (UOT, UMOT, also: acousto-optic tomography, AOT), the tissue sample is irradiated by a coherent light source, and concurrently an ultrasound wave is focused inside the object. See Figure 2.2 for an illustration of the setup in UOT. It has been found that a part of the optical signal is modulated at the frequency of ultrasound [35, 62]. The intensity of this modulation relates to the photon density at the location of the ultrasound focus. Multiple experiments are conducted in which the ultrasound focus is scanned throughout the medium, so that information about the photon density at each location inside the object can be obtained. Reconstructing the distribution of optical properties from this type of interior data is known to be significantly less ill-posed than reconstruction from the boundary measurements collected in conventional optical tomography. Modulation by ultrasound in some sense provides an interior excitation without physically accessing the object's interior.

2.1.3. History of ultrasound modulated optical imaging

Ultrasound tagging of photons in the optical spectrum for the purpose of imaging was first discussed by Marks et al. in 1993 [41]. Wang et al. [61] presented experimental results of optical imaging with continuous-wave ultrasound modulation. Experimental results were supplemented with theoretical explanations of the modulation effect by Leutz and Maret [35]. In 1997 Kempe et al. [25] analytically and experimentally investigated optical imaging by modulation with narrowly focused ultrasound signals.

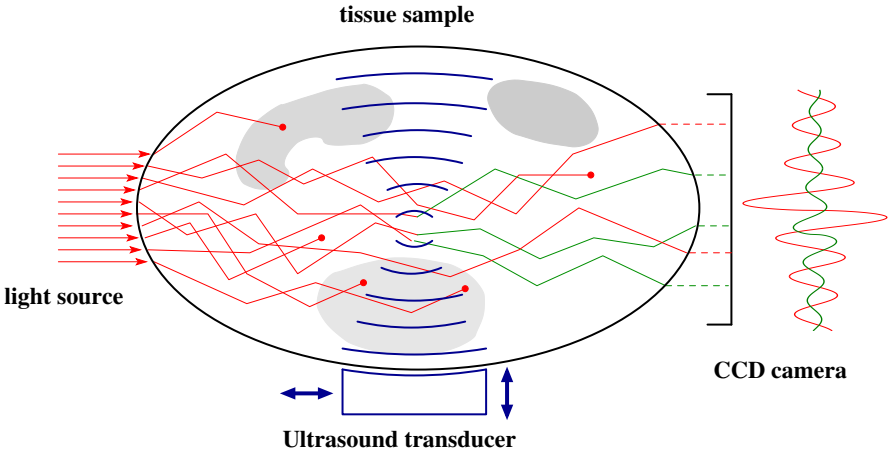

Fig. 2.2. Setup in ultrasound modulated optical tomography.

In 2001 Wang proposed analytic and Monte Carlo models for UOT [58, 59]. Since then, UOT has seen numerous improvements in signal acquisition techniques and experimental setup. However, most of the existing techniques are based on direct imaging, using the measurements of modulation intensity to represent the optical properties near the ultrasound focus.

The only work known to the author that attempts to reconstruct actual optical material parameters from UOT measurements with focused ultrasound is the thesis of Nam [43]. However, this work assumes internal light intensities to be known and does not incorporate the process of ultrasound modulation into the mathematical model. We intend to close this gap by proposing a model for UOT that includes the process of ultrasound modulation as well as the measurements, and is based on the diffusion approximation for light propagation in highly scattering media.

2.1.4. Diffusion model for ultrasound modulation

The literature contains a number of models that address the UOT technique, see for example [25, 35, 43, 59, 60, 62]. Most of them describe the coupling between ultrasound and light in probabilistic terms. The path of individual photons is modeled as a stochastic process, and the influence of the ultrasound signal on the probabilities for photons to be scattered or absorbed is investigated. For practical purposes, this allows particle-based Monte Carlo simulations of the light intensity modulation effect caused by the ultrasound wave.

On the other hand, for optical imaging in turbid media at a depth of centimeters, photon intensities can be accurately modeled by the diffusion approximation. The diffusion model consists of a partial differential equation (PDE), whose solution describes the photon density inside the tissue sample. Under certain assumptions, the stochastic description of the coupling between ultrasound signal and photon intensity can be translated to the diffusion regime. It will be shown in Section 2.2 that this leads to a set of coupled diffusion equations describing the original light intensity and a second, virtual intensity field that represents the part of the optical signal that is modulated by ultrasound. The problem of reconstructing optical tissue properties from UOT measurements then yields a parameter identification problem for two coupled PDEs. Since numerical techniques for solving elliptic PDEs are well developed and highly efficient, it can be hoped that this approach leads to fast reconstruction schemes for UOT that do not need to resort to statistical sampling for evaluating probabilistic models of photon propagation.

2.1.5. Outline

The mathematical principles of ultrasound modulation of coherent light in turbid media are discussed in Section 2.2. We then derive a model for the effect of ultrasound modulation in the diffusion regime, describe the measurement process in UOT and introduce the parameter identification problem that arises for reconstruction of the absorption coefficient. In Section 2.3, three simple computational algorithms are derived for reconstructing the spatially varying absorption coefficient from scanning UOT measurements with well-focused ultrasound signals. Examples of the resulting reconstructions from numerical phantom data are provided in Section 2.4.

The most problematic assumption in our reconstruction scheme is the perfect focusing of ultrasound, which is unrealistic for practical applications. Section 2.5 discusses synthetic focusing techniques that allow focused measurements to be recovered from measurements with ultrasound localized along lines or spheres.

Given the simplicity of our computational reconstruction schemes and the lack of regularization, the high quality of the obtained absorption images for numerical phantoms suggests that the reconstruction problem at hand must be rather well-posed, or at least is not as ill-posed as the conventional OT reconstruction problem. In Section 2.6, a formal linearization of our model is studied that relates perturbations in the absorption coefficient and in the measurements by a Fredholm operator between appropriately chosen Sobolev spaces. This provides a partial explanation to the stable reconstruction observed in the numerical experiments. The last section concludes with a summary and possible directions for future research on the topic.

2.2. Mathematical model

In this section, we first give a brief overview of the principles that govern ultrasound modulation of light in turbid media, and describe the quantities that are being measured in UOT. After some rearrangements, this leads to the description of a virtual light source of photons tagged by the ultrasound signal. We use this observation to derive a model for ultrasound modulation in the diffusion regime of photon propagation. We describe the measurements in terms of our model, and formulate an inverse problem for the reconstruction of optical absorption from UOT measurements with scanning of the ultrasound signal.

2.2.1. Principles of ultrasound modulation

Three mechanisms for ultrasound modulation of light in tissue have been identified in the literature [59]:

1. Variations in optical properties induced by ultrasound. The ultrasound wave causes tissue cells to compress and expand periodically, changing the index of refraction, scattering and absorption rates. This in turn influences photon propagation and leads to partial modulation of the measured light signal at ultrasound frequency.

2. Variations of optical phase by ultrasound induced oscillation of scatters. Scattering sites undergo periodic motion caused by ultrasound which affects the scattering paths of photons. This leads to oscillation of the optical phase at ultrasound frequency which can be detected in the measurements.

3. Variations of optical phase by ultrasound modulation of index of refraction. Similar to the second mechanism, periodic changes of the refractive index cause modulation of the optical phase at ultrasound frequency.

The second and third mechanism require a coherent light signal, while coherence is not necessary for the first mechanism. Since ultrasound modulation of non-coherent light has been found to be weak in experiments [59, 60], it is believed that the dominant cause for ultrasound modulation of coherent light is given by the second or third effect. Hence, our derivation will be based on results that have been established for coherent light [25, 35, 59]. However, we note that there exist descriptions of the UOT procedure based on the first mechanism [40] and that these result in mathematical models that are considerably different from the one discussed here [9]. For ultrasound modulation of coherent light, it was shown in [59] that the second and third mechanisms yield the same type of analytical model. A brief discussion of this model is given in the following.

A plane ultrasound wave irradiates a homogeneous isotropic medium that occupies a domain Ω. Let $\eta \in \partial\Omega$ denote the location of a detector for optical light. It is assumed that the optical wavelength is much shorter than the mean free path between scattering events (*weak scattering*). In practice, the optical wavelength is about 700 nm, and in soft tissue the typical scattering mean free path is about 1 mm, so that this assumption is satisfied. Also we require that variations in optical path length induced by the ultrasound signal are much smaller than the optical wavelength (*weak modulation*).

The signal that is measured, e.g. by an interferometer, is the electric field autocorrelation function at η [35]:

$$G_1(\eta, \tau) = \langle E(\eta, t+\tau) E^*(\eta, t) \rangle_t$$

Here angle brackets denote averaging over time, and the electric field E is related to the light intensity I as $I(\eta, t) = |E(\eta, t)|^2$. It has been shown experimentally (see [35]) that on short time scales the autocorrelation function oscillates at ultrasound frequency (typically between 1 and 20 MHz). Over time scales much longer than the ultrasound period, coherence of the exiting light is lost, i.e. $G_1(\eta, \tau) \to 0$ as $\tau \to \infty$, due to the Brownian motion of scatteres. Since we are interested in the ultrasound modulation part of the autocorrelation, all terms arising from the decay due to Brownian motion will be neglected in the following discussion. We will derive expressions for G_1 and, in particular, its *modulation depth*, i.e. the magnitude of the oscillation of G_1 at ultrasound frequency.

2.2.2. A path integral model

For a point source of unit strength at location $\sigma \in \Omega$, its contribution to the overall autocorrelation at η can be written as

$$G_1(\sigma, \eta, \tau) = \sum_{s=s(\sigma,\eta)} P_s \langle E_s(t+\tau) E_s^*(t) \rangle_t .$$

The sum extends over all scattering paths s inside Ω that connect source σ and boundary location η. P_s is the fraction of the intensity incident at σ that scatters along s multiplied by the probability of a photon not getting absorbed along this

path. E_s denotes the accumulated phase of the electric field at η from photons following path s. Consequently, $\langle E_s(t)E_s^*(t)\rangle_t = 1$, and $G_1(\sigma,\eta,0)$ is the probability of photons originating at σ to reach the detector at η.

In [25, 59] it was shown how autocorrelation is influenced by an ultrasound pressure wave with frequency ω_a through mechanisms 2 and 3 mentioned above. If we neglect contributions from Brownian motion of the scatterers, it follows from [25] that

$$G_1(\sigma,\eta,\tau) = \alpha \int_\Omega P(\sigma,x)P(x,\eta)|p(x)|^2(1-\cos\omega_a\tau)\,dx,$$

where $|p(x)|$ is the amplitude of the ultrasound signal at x, $P(x,y)$ is the probability of photons originating at x to reach y, and α is a proportionality constant. In particular, the dependence on the square of the ultrasound amplitude has been observed experimentally, see [35].

Since $P(x,y) = G_1(x,y,0)$, we can rewrite the previous equation as

$$G_1(\sigma,\eta,\tau) = \alpha \int_\Omega G_1(\sigma,x,0)G_1(x,\eta,0)|p(x)|^2(1-\cos\omega_a\tau)\,dx.$$

If light is incident with intensity $S(\sigma)$ from boundary sources at positions $\sigma \in \partial\Omega$, the overall autocorrelation function at detector location η is

$$G_1(\eta,\tau) \;\; = \textstyle\int_{\partial\Omega} S(\sigma)G_1(\sigma,\eta,\tau)\,d\sigma.$$

Using the previous equation, and defining the unmodulated light intensity $u(x) =$

$\int_{\partial\Omega} S(\sigma)G_1(\sigma, x, 0)\, d\sigma$ for all $x \in \Omega \cup \partial\Omega$, we find that

$$\begin{aligned} G_1(\eta, \tau) &= \alpha \int_\Omega u(x)|p(x)|^2 G_1(x, \eta, 0)\, dx\ (1 - \cos\omega_a \tau) \\ &= v(\eta)(1 - \cos\omega_a \tau), \end{aligned}$$

where

$$v(\eta) = \alpha \int_\Omega u(x)|p(x)|^2 G_1(x, \eta, 0)\, dx. \tag{2.1}$$

This representation of the correlation has given rise to the name *tagged photons* or *virtual light source* for v. Equation (2.1) implies that these tagged photons originate at the site x of interaction of the unmodulated light intensity $u(x)$ and ultrasound field $p(x)$. For detector locations η close to the focus of the ultrasound signal, the presence of the virtual source v has been observed experimentally [62]. However, technically v is not an actual photon flux but a (scaled) correlation function.

2.2.3. Diffusion based model of ultrasound modulation

Now that we have derived expressions that quantify the effect of ultrasound modulation, we need to relate them to the optical properties of the medium. To this end, we need a model for describing photon propagation in soft tissue. A very general analytic model for photon propagation inside a medium is given by the *radiative transfer equation* (RTE, also: Boltzmann equation). The RTE is a partial differential equation for the *radiance*, i.e. the energy flux per direction at each point inside the medium (see [62] for a detailed description of the RTE). Since the radiance in 3D depends on six independent variables, namely location inside the medium, direction of energy flux and time, it is difficult to treat numerically. Hence, there exist

several simpler models that approximate solutions to RTE to various degrees of accuracy under certain assumptions. See [7] for an overview of approximate models. A commonly used model is the *diffusion approximation*, which is appropriate if the medium is strongly scattering, isotropic and if photons on average experience sufficiently many scattering events. These conditions are satisfied for many types of soft tissue [7]. Under the diffusion approximation, the steady state unmodulated light intensity $u(x) = \int_{\partial\Omega} S(\sigma)G_1(\sigma, x, 0)\, d\sigma$ satisfies the *diffusion equation*:

$$-\nabla \cdot D\nabla u(x) + \mu_a u(x) = 0 \qquad \text{in } \Omega. \tag{2.2}$$

Here, $\mu_a = \mu_a(x)$ is the spatially varying absorption coefficient,

$$D = D(x) = \frac{1}{3(\mu_a(x) + \mu_s'(x))} \tag{2.3}$$

is the diffusion coefficient and μ_s' the reduced scattering coefficient. In highly scattering media, $\mu_s' \gg \mu_a$, and the diffusion coefficient is dominated by scattering. In this text, we restrict our interest to the reconstruction of the absorption coefficient μ_a, since it can express various structural and functional anomalies in soft tissue [14]. Hence we will consider μ_s' to be approximately constant in the following. However, we note that in principle the model presented here could just as well be used for reconstruction of the scattering coefficient.

Equation (2.2) is complemented by boundary conditions. For tissue in contact with a surrounding medium, Robin-type boundary conditions are a common choice [7]:

$$2D\frac{\partial u(x)}{\partial n} + \gamma u(x) = S(x) \qquad \text{on } \partial\Omega. \tag{2.4}$$

Here n denotes the outward normal to the surface $\partial\Omega$ and $\gamma > 0$ is a constant describing the optical refractive index mismatch at the boundary.

From (2.2), (2.4) and the definition of u, we conclude that $G_1(\cdot,\cdot,0)$ is the Green's function for the diffusion equation with Robin boundary condition, and hence satisfies the equations

$$-\nabla_x \cdot D\nabla_x G_1(x,y,0) + \mu_a G_1(x,y,0) = \delta(x-y) \qquad \text{for all } \ x,y \in \Omega, \quad (2.5)$$

$$2D\frac{\partial G_1(x,y,0)}{\partial n_x} + \gamma G_1(x,y,0) = 0 \qquad \text{for } \ x \in \partial\Omega, y \in \Omega. \quad (2.6)$$

Here, δ denotes the Dirac delta distribution. We note that if photon propagation in a medium is viewed as a random walk, then the interpretation of the transition probability $P(x,y) = G_1(x,y,0)$ as the Green's function for a diffusion equation is quite common.

Finally, from equations (2.1), (2.5) and (2.6) it follows that v is a solution to the following boundary value problem:

$$\begin{cases} -\nabla \cdot D\nabla v(x) + \mu_a v(x) = \alpha|p(x)|^2 u(x) & \text{in } \ \Omega, \\ 2D\frac{\partial v(x)}{\partial n} + \gamma v(x) = 0 & \text{on } \ \partial\Omega. \end{cases} \quad (2.7)$$

This agrees with the intuitive notion of viewing v as a virtual light source of ultrasound tagged photons. Together with (2.2) and (2.4), these equations form our model for ultrasound modulation of coherent light in soft tissue.

2.2.4. Measurements

Detectors. We will assume that the amplitude $v(\eta)$ of the oscillation of $G_1(\eta, \tau)$ at ultrasound frequency can be measured directly. Since the frequency of ultrasound ω_a and autocorrelation time shift τ are known in controlled experiments, this poses no restriction, but it will simplify the following discussion.

In principle, interferometric detectors could be placed around the entire boundary to pick up $v(x)$. In practice, however, we will only be able to measure at a small number of locations. To simplify the discussion, we will assume that only a single detector at location $\eta \in \partial\Omega$ is used. More elaborate experimental setups could include multiple detectors to suppress the effects of noise.

Ultrasound scanning. Equation (2.7) holds for arbitrary ultrasound functions $p(x)$. The shape of the ultrasound function can be controlled by the experimental setting. Hence, additional measurement data can be obtained by conducting multiple experiments with different shapes of the ultrasound function. In particular, it can be attempted to focus the ultrasound signal to a specific part of Ω. It is clear from (2.7) that the obtained measurement will then only depend on the values of u within the focal region of the ultrasound. By scanning the ultrasound throughout Ω, complementary information about u in different parts of the domain can be collected. More generally we can assume that the data consists of measurements of $v^\xi(\eta)$ corresponding to ultrasound signals p^ξ from a set $\{p^\xi\}_{\xi \in I}$ indexed by $\xi \in I$.

2.2.5. The reconstruction problem

We can now formulate the reconstruction problem addressed in this work:

Inverse problem formulation. *Given a family of ultrasound signals* $\{p^\xi\}_{\xi\in I}$*, the light illumination pattern* $S(x)$*, detector location* $\eta \in \partial\Omega$*,* μ_s' *and* γ*. Assume that for each* $\xi \in I$*, the values*

$$h(\xi) = v^\xi(\eta) \tag{2.8}$$

are known in the coupled system of equations

$$\begin{cases} -\nabla \cdot D\nabla u(x) + \mu_a u(x) = 0 & \text{in } \Omega, \\ 2D\frac{\partial u(x)}{\partial n} + \gamma u(x) = S(x) & \text{on } \partial\Omega, \\ -\nabla \cdot D\nabla v^\xi(x) + \mu_a v^\xi(x) = \alpha |p^\xi(x)|^2 u(x) & \text{in } \Omega, \\ 2D\frac{\partial v^\xi(x)}{\partial n} + \gamma v^\xi(x) = 0 & \text{on } \partial\Omega. \end{cases} \tag{2.9}$$

The goal is to recover the spatially varying absorption coefficient μ_a *inside a region of interest* $U \subset \Omega$*.*

Naturally, any question about existence and uniqueness of solutions or the well-posedness of the above problem is tightly related to the choice of the ultrasound signals $\{p^\xi\}_{\xi\in I}$. If, for example, the data consisted only of one measurement for a single ultrasound signal, there is no hope of recovering the spatially varying coefficient on any open set.

On the other hand, if the ultrasound beam is focused to a point $\xi \in \Omega$, the measurement $v(\eta)$ will depend on the value of $u(x)$ at $x = \xi$ only. In practice, due to the wave nature of ultrasound it is impossible to focus to a single point [36]. Nonetheless, the assumption of perfectly focused ultrasound is common in the

literature.

Hence we assume in the following two sections that scanning measurements are available for perfectly focused ultrasound signals, i.e. that

$$|p^{\xi}(x)|^2 = \delta(x-\xi), \qquad \xi \in U$$

and the measurements are

$$h(\xi) = v^{\xi}(\eta) \qquad \text{for all } \xi \in U.$$

In the next section, some simple computational reconstruction schemes for recovering μ_a from such measurements are discussed. Some ideas for reconstruction from measurements with non-focused ultrasound signals will be presented in Section 2.5.

2.3. Reconstruction

2.3.1. Reconstruction formula for scanning measurements with focused ultrasound

The purpose of this section is to show that under the model (2.9), high resolution reconstruction of the absorption from scanning measurements with focused ultrasound is feasible. The algorithm discussed here is conceptually simple but still yields reasonable results as we shall see in Section 2.4. Throughout this section we assume that ultrasound signals can be perfectly focused to any point inside Ω, i.e. $|p^{\xi}(x)|^2 = \delta(x-\xi)$ and $h(\xi)$ is available for all $\xi \in U$.

Let $G(x,y)$ denote Green's function for the diffusion model (2.2), i.e. the solution

of

$$\begin{cases} -\nabla_x \cdot D\nabla_x G(x,y) + \mu(x)G(x,y) = \delta(x-y) & x \in \Omega, \\ 2D\frac{\partial G(x,y)}{\partial n_x} + \gamma G(x,y) = 0 & x \in \partial\Omega. \end{cases} \tag{2.10}$$

By definition of Green's function, the solution v^ξ in (2.9) can be written as

$$\begin{aligned} v^\xi(x) &= \int_\Omega G(x,y)\alpha|p^\xi(y)|^2 u(y)\,dy \\ &= \alpha\int_\Omega G(x,y)\delta(\xi-y)u(y)\,dy \\ &= \alpha G(x,\xi)u(\xi). \end{aligned} \tag{2.11}$$

Thus,

$$h(\xi) = v^\xi(\eta) = \alpha G(\eta,\xi)u(\xi), \qquad u(\xi) = \frac{h(\xi)}{\alpha G(\eta,\xi)}. \tag{2.12}$$

Substituting (2.12) into the first equation of (2.9), we obtain an equation for recovering μ_a:

$$\mu_a(\xi) = \frac{[\nabla_\xi \cdot D\nabla_\xi]\,(h(\xi)/G(\eta,\xi))}{h(\xi)/G(\eta,\xi)}. \tag{2.13}$$

2.3.2. Reconstruction algorithms

The obvious problem in using formula (2.13) for reconstruction is that it is implicit in μ_a since both D and the Green's function G depend on the absorption. Three approaches to deal with this issue are given in the following algorithms:

- **Algorithm 1.** Instead of the exact Green's function G, use an approximation $\widetilde{G}$ in (2.13). For example, for constant absorption $\mu_a(x) = \bar{\mu}_a$ and constant diffusion $D(x) = \bar{D}$, the whole space Green's function to (2.2) on $\mathbb{R}^d$ is given

by

$$\widetilde{G}(x,y) = \begin{cases} \frac{1}{2\pi} K_0\left(\kappa|x-y|\right) & d=2, \\ \frac{1}{4\pi|x-y|} \exp\left(-\kappa|x-y|\right) & d=3, \end{cases}$$

where $\kappa = \sqrt{\bar{\mu}_a/\bar{D}}$ and K_0 is the modified Bessel function of the second kind [6].

- **Algorithm 2.** For given $\bar{\mu}_a$ and $\bar{D}$, an approximation to Green's function can be computed by solving (2.10) numerically.

- **Algorithm 3.** The previous algorithm can be iterated to compute successively refined reconstructions for μ_a:

  - **Initial step**: Using an initial guess μ_a^0 for the absorption coefficient (e.g. $\mu_a^0 = const$), compute the corresponding Green's function numerically, and apply formula (2.13) to find a new approximation μ_a^1.
  - **Iterative step:** Using the current approximation μ_a^k, recompute Green's function and D and apply formula (2.13) to find μ_a^{k+1}.

The Green's function used in Algorithm 1 neither incorporates the correct absorption coefficient nor satisfies the boundary conditions posed in (2.10). Hence, we cannot expect the resulting reconstruction to be quantitatively correct or even qualitatively correct near the boundary of Ω. In Algorithm 2, the numerical Green's function satisfies the correct boundary condition and we can expect reconstructions to be at least qualitatively valid. The iterative Algorithm 3 has the potential of successively approximating the correct Green's function and hence we can hope for quantitatively correct reconstructions after sufficiently many iterations.

Although we do not investigate the convergence properties of the iterative scheme here, in the numerical simulations presented in the following section the iterates converged reliably, albeit slowly.

2.4. Numerical implementation

In this section, numerical tests are performed using the algorithms outlined in the previous section. We first state the computational setting and outline the calculations involved in simulating the forward problem and the measurement process. Then the implementation of the reconstruction schemes is discussed. Finally, we introduce the particular test cases for our computations and present the results.

In this text, we only use synthetic measurement data obtained by forward calculations from mathematical phantoms, rather than actual experimental data. All computations were done in 2D, although they can be readily carried over to 3D. For the finite element calculations involved in solving boundary value problems for diffusion equations, the open source finite element library deal.II [10, 11] was used.

2.4.1. Computational setting

We take Ω to be the square $[0\text{ cm}, 5\text{ cm}]^2$, which approximately corresponds to the relevant dimensions in a practical UOT setting. The reconstruction domain U is chosen as $[0.5\text{ cm}, 4.5\text{ cm}]^2$. For the boundary light source S in (2.4), $\partial\Omega$ is split into $\partial\Omega_1 = \{x \in \partial\Omega : x_1 = 0\text{ cm}\}$ and $\partial\Omega_2 = \partial\Omega \setminus \partial\Omega_1$. Constant illumination is assumed

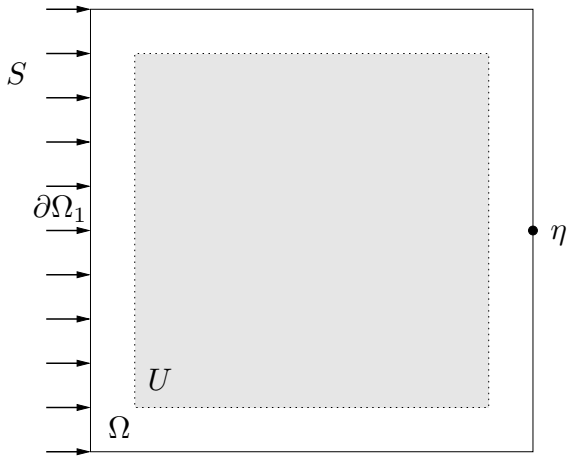

Fig. 2.3. Setting for numerical experiments: Domain Ω, area of interest U, incident light source $S(x)$ on the left, and detector point η on the right.

on $\partial\Omega_1$ and no photons are injected on $\partial\Omega_2$:

$$S(x) = \begin{cases} 1 & \text{for} \quad x \in \partial\Omega_1, \\ 0 & \text{for} \quad x \in \partial\Omega_2. \end{cases} \tag{2.14}$$

The modulation depth is measured at a single detector location $\eta = (5 \text{ cm}, 2.5 \text{ cm})$. This layout is depicted in Figure 2.3.

2.4.2. Numerical test cases

Ultrasound field. In our numerical examples, we use Gaussian-shaped synthetic ultrasound signals:

$$p(x) = C \exp\Big(- \sum_{j=1}^{d} \frac{|x_j|^2}{\sigma_j^2} \Big), \tag{2.15}$$

where C is a normalization constant. By choosing different variances σ_j^2, we can model the focusing properties of the pressure field.

To simulate scanning of the ultrasound focus, focusing points $\{\xi^i,\ i = 1, \ldots, N\}$ are placed at the vertices of a regular square grid covering the area of interest U. For each i we then construct a signal $p^{\xi^i}(x)$ focused at ξ^i by setting

$$p^{\xi^i}(x) := p(x - \xi^i).$$

To simplify notation we set $v^i := v^{\xi^i}$ and $p^i := p^{\xi^i}$ in the following.

Absorption phantoms. To test our algorithms, we use three test cases in which the true absorption coefficients have the following form:

- A disk-shaped inclusion $K \subset \Omega$ with midpoint $(2.5\text{ cm}, 2.5\text{ cm})$ and radius 0.5 cm. The absorption coefficient is assumed to be equal to $\bar{\mu}$ outside the inclusion and slightly higher inside:

$$\mu^*(x) = \begin{cases} \bar{\mu} \quad , & x \in \Omega \setminus K \\ 1.2\,\bar{\mu}\ , & x \in K. \end{cases}$$

- For the same inclusion K, a much higher absorption coefficient contrast is chosen:

$$\mu^*(x) = \begin{cases} \bar{\mu} \quad , & x \in \Omega \setminus K \\ 10\,\bar{\mu}\ , & x \in K. \end{cases}$$

- A more complicated coefficient with multiple inclusions of different magnitude between $1.2\,\bar{\mu}$ and $2.0\,\bar{\mu}$. Their exact shape is shown in the right panel of Figure 2.4. This case tests the ability of our algorithms to resolve several

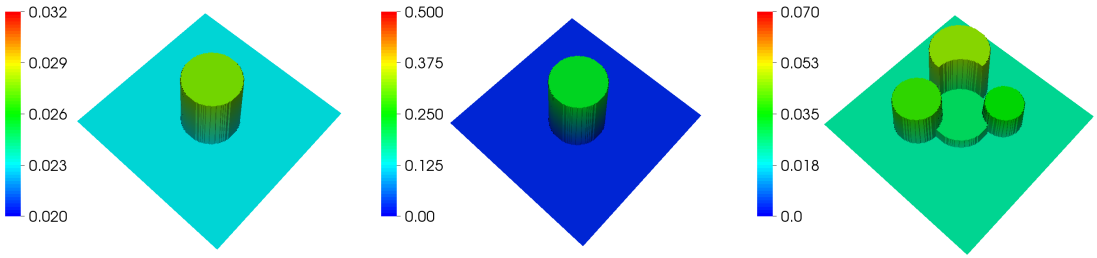

Fig. 2.4. Test cases for absorption coefficient μ^*.

nearby objects.

For actual numerical values, we used $\bar{\mu} = 0.023$ cm^{-1}, $\mu_s' = 10.74$ cm^{-1} and $\gamma = 0.431$ cm^{-1} in our computations. These values represent typical optical properties of soft tissue [42].

2.4.3. Forward simulations

In order to generate artificial measurements $h(\xi)$ (see (2.8)), we need to compute the solutions $u(x), v^\xi(x)$ of the forward problem (2.9) for a set of given data D, μ_a, S (diffusion coefficient, absorption coefficient, incoming light flux) and an ultrasound signal focused at the point $\xi \in U$. Then, evaluating v^ξ at the detector location η, we obtain the measurement value $h(\xi)$.

Incident light field. Since in our model the incident light intensity u is independent of the shape and location of the ultrasound wave, u only needs to be computed once. For this computation, a finite element approximation to u is constructed on a regular rectangular grid using $\mathbb{Q}_1$ finite elements [13], solving equations (2.2)–(2.4).

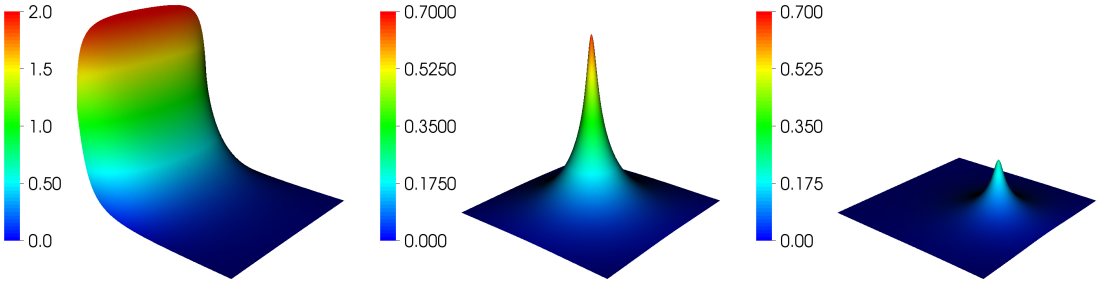

Fig. 2.5. Left: Incident light intensity u for constant absorption coefficient. Center and right: Modulated light intensity v^ξ for two different focus points ξ. Note that v depends on the focus position as well as the intensity of u at the focus.

The left panel of Figure 2.5 shows u for the case of a constant absorption coefficient μ_a.

Modulated light field and measurements. Given u and the choice of ultrasound signal p^i, we compute the intensity of the modulated light $v^i(x)$ using equations (2.9). The equations are again solved using $\mathbb{Q}_1$ finite elements. Two examples for v^i are shown in Figure 2.5 for two different focus positions. The modulated light intensities v^i are then evaluated at the sensor location η to yield the measurements $h(\xi^i) = v^i(\eta)$.

2.4.4. Green's function and reconstruction

The reconstruction Algorithms 2 and 3 require knowledge of the Green's function G, which, given the absorption and diffusion coefficients μ_a and D, solves (2.10). Hence, we compute G by solving another diffusion problem with homogeneous Robin boundary conditions and a suitable approximation to the delta function as the right

hand side. As before, this is done using a finite element scheme, where we choose a different, coarser mesh than in forward problem calculations to avoid committing inverse crimes.

An obvious problem in the reconstruction formula (2.13) is that it involves derivatives of the measurement data $h(\xi)$, which causes instabilities in the presence of noise. Regularizations for this type of problem are well-studied (e.g. [43]), and the stability analysis in Section 2.6 suggests that this is the only source of instability in the reconstruction process. Hence, we opt not to add extra regularization and compute the derivatives by a simple central differencing scheme. Without adding noise to the measurements, it turned out that in all of our computational experiments, the regularization stemming from discretization on a fixed grid was sufficient for obtaining reconstructions without visible noise artifacts.

2.4.5. Reconstruction results

For the results shown in this section, measurements were produced using the ultrasound signal arising from setting variances $\sigma_1 = \sigma_2 = 0.1$ cm in the Gaussian (2.15), resulting in sharp focusing in each direction (see the center panel of Figure 2.8 on page 33). The ultrasound focus ξ^i was scanned on a 100×100 mesh of points inside the area of interest U. Figure 2.6 shows reconstructions obtained from each of the three algorithms from Section 2.3.2 for the three different cases of absorption phantoms.

To estimate if the reconstructed coefficients are quantitatively correct, profiles of the reconstructions along lines were extracted and plotted in Figure 2.7 for each

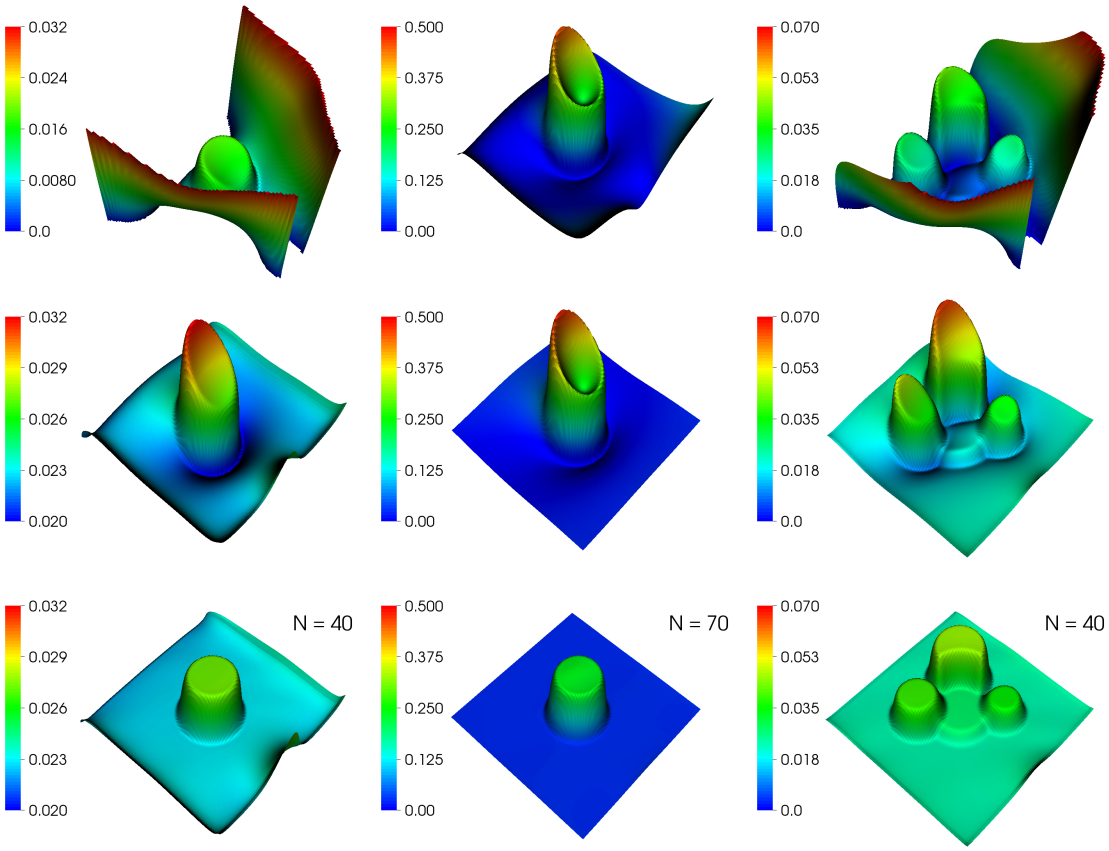

Fig. 2.6. Reconstruction results for the three coefficient phantoms: Algorithm 1 (top), Algorithm 2 (middle), Algorithm 3 after $N = 40, 70$ and 40 iterations, respectively (bottom).

of the three phantoms.

The results confirm the expectations stated in Section 2.3.2:

- Algorithm 1 produces reconstructions that are incorrect especially near the boundary of the domain, but somewhat hint at the location of interior singularities, especially in the case of large variations in the coefficient.
- Reconstructions from Algorithm 2 are not quantitatively correct but capture the locations of singularities in the coefficient.
- Algorithm 3 after sufficiently many iterations produced correct reconstructions for all three phantoms. Reconstruction are slightly off near the sensor location $\eta = (5 \text{ cm}, 2.5 \text{ cm})$ in the cases of small coefficient variation and multiple inclusions.

In particular, Algorithm 3 reconstructs sharp interfaces between inclusions without excessive blurring and recovers quantitatively correct values of the absorption coefficient. These are significant advantages in comparison to many other optical tomographic methodologies.

2.5. Ultrasound focusing

So far we have assumed that ultrasound can be perfectly focused to individual points inside the object of interest. In practice, this is not a realistic assumption: Diffraction due to the wave nature of ultrasound and the geometry and bandwidth of the transducer limit the achievable focus size. In particular, the focus is often much sharper in the direction transverse to the transducer lens, but elongated and blurred

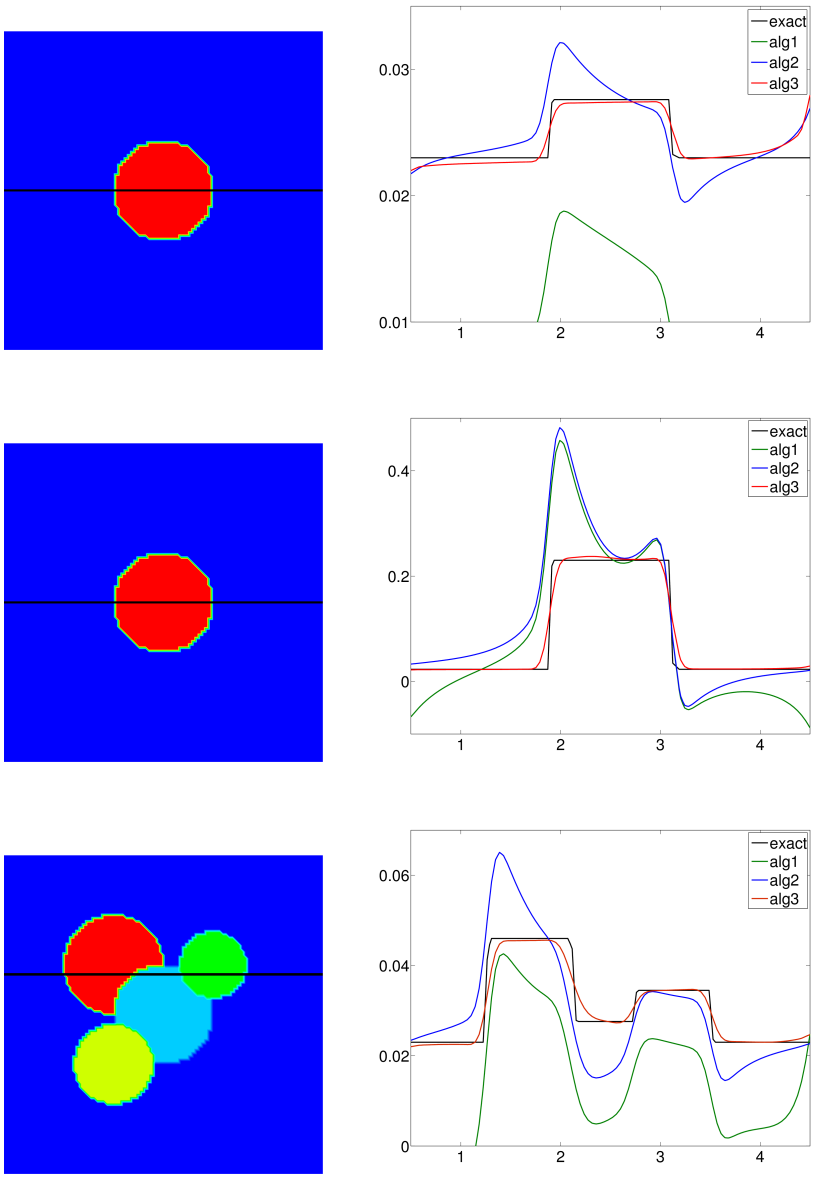

Fig. 2.7. Reconstruction profiles (right) along lines (left). Phantom with small variations (top), large variations (middle) and multiple inclusions (bottom). Profiles show exact coefficient (black, interpolated on the finite element grid), reconstructions from Algorithm 1 (green), Algorithm 2 (blue) and Algorithm 3 (red).

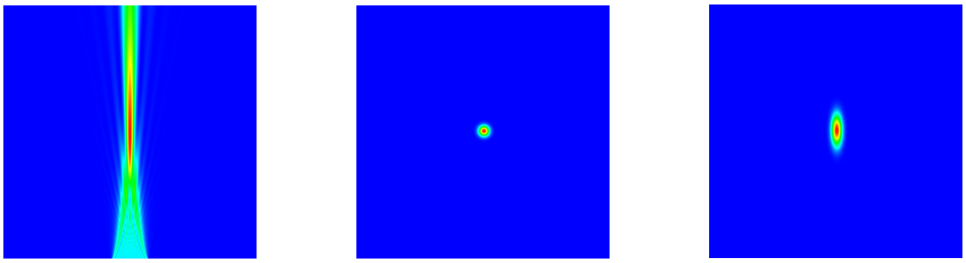

Fig. 2.8. Simulated ultrasound pressure field $|p|^2$ with transducer at the bottom (left), Gaussian ultrasound signal $|p|^2$ with $\sigma_1 = \sigma_2 = 0.1$ (center), Gaussian signal with $\sigma_1 = 0.1$, $\sigma_2 = 0.3$ (right).

along the transducer direction. A realistic simulation of a focused ultrasound beam is shown in the left panel of Figure 2.8 (see [3] for the details of this simulation). Experimental measurements of focused ultrasound signals can be found e.g. in [36]. For a comprehensive discussion of localization of waves see [22].

To demonstrate that sharp ultrasound focusing is a crucial requirement for the reconstruction algorithms presented in Section 2.3, the computational experiments from Section 2.4 were repeated with a Gaussian ultrasound signal that is slightly elongated in transducer direction. This signal is shown in the right panel of Figure 2.8. For comparison, the ultrasound signal used in Section 2.4 is shown in the center panel of Figure 2.8.

Figure 2.9 shows the results produced by Algorithms 2 and 3. The quality of reconstruction is severely deteriorated, sharp interfaces are blurred especially in y-direction, and the reconstructed absorption has spurious peaks near the domain boundaries and the detector location. It is clear that reconstructions from scanning measurements with a realistic, even more elongated ultrasound signal (such as Fig-

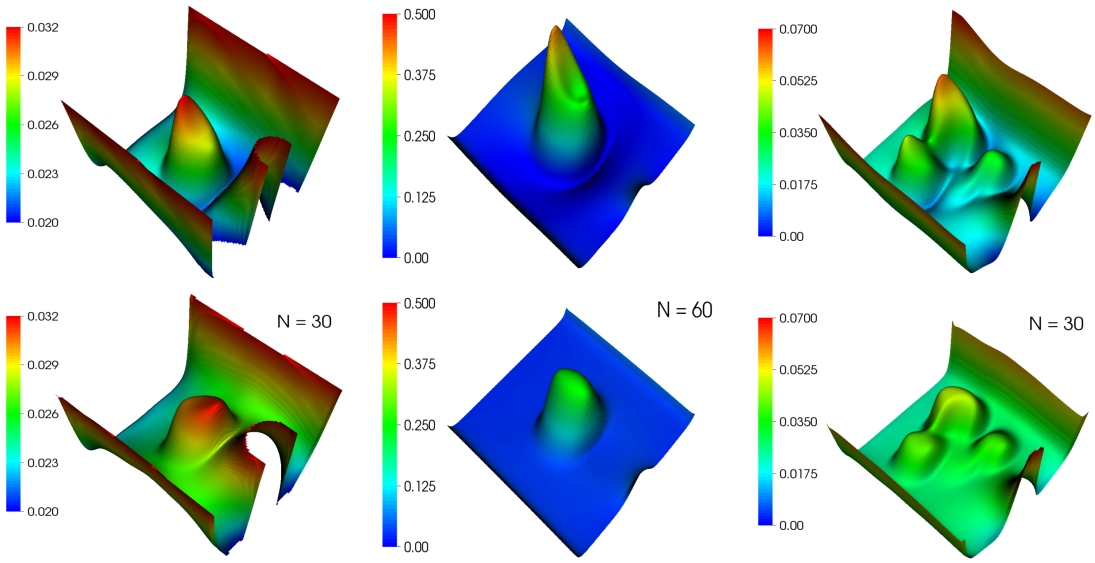

Fig. 2.9. Reconstruction results for ultrasound signal with elongated focus: Algorithm 2 (top) and after N iterations of Algorithm 3 (bottom).

ure 2.8, left) would be even worse. Hence, strategies need to be developed to deal with measurements obtained from ultrasound modulation without perfect focusing. One of these strategies, known as *synthetic focusing*, is discussed in the following.

2.5.1. Synthetic focusing principle

Instead of attempting to perfectly focus ultrasound waves in space, *synthetic focusing* allows the use of non-localized ultrasound fields and reconstructs the signal by superposition. This approach was suggested in [30]. The idea is that if measurements are obtained from a specifically chosen set of non-focused ultrasound signals, a mathematical reconstruction procedure can recover what the measurements from focused ultrasound signals would have been. This reconstruction procedure involves

the inversion of an integral transform.

To explain the details of this technique for UOT, let us assume that measurements are obtained for a set $\{p^\lambda\}_{\lambda\in\Lambda}$ of non-focused ultrasound signals. This means that the measurements are $h^\lambda = v^\lambda(\eta)$, where v^λ solves

$$\begin{aligned} -\nabla\cdot D\nabla v^\lambda(x) + \mu_a v^\lambda(x) &= \alpha|p^\lambda(x)|^2 u(x) && \text{in } \Omega, \\ 2D\frac{\partial v^\lambda(x)}{\partial n} + \gamma v^\lambda(x) &= 0 && \text{on } \partial\Omega \end{aligned} \tag{2.16}$$

for all $\lambda\in\Lambda$. As before, $u(x)$ is the unmodulated light intensity, the solution to (2.2) and (2.4).

On the other hand, the input that is required for the algorithms in Section 2.3 is $h^\xi = v^\xi(\eta)$ for all $\xi\in U$, with v^ξ solving

$$\begin{aligned} -\nabla\cdot D\nabla v^\xi(x) + \mu_a v^\xi(x) &= \alpha\delta(x-\xi)u(x) && \text{in } \Omega, \\ 2D\frac{\partial v^\xi(x)}{\partial n} + \gamma v^\xi(x) &= 0 && \text{on } \partial\Omega. \end{aligned}$$

We observed in (2.11) that

$$v^\xi(x) = \alpha G(x,\xi)u(\xi).$$

Since the v^λ solve the diffusion problem (2.16), they can be written as a convolution of Green's function with the right hand side:

$$\begin{aligned} v^\lambda(x) &= \int_\Omega G(x,\xi)\alpha|p^\lambda(\xi)|^2 u(\xi)\,d\xi \\ &= \int_\Omega \Big(\alpha G(x,\xi)u(\xi)\Big)|p^\lambda(\xi)|^2\,d\xi \\ &= \int_\Omega v^\xi(x)|p^\lambda(\xi)|^2\,d\xi. \end{aligned}$$

Hence,

$$h^\lambda = v^\lambda(\eta) = \int_\Omega v^\xi(\eta)|p^i(\xi)|^2\,d\xi = \int_\Omega h(\xi)|p^\lambda(\xi)|^2\,d\xi. \tag{2.17}$$

This equation implies that the measurements h^λ are derived from the focused data $h(\xi)$ by integration against the squared amplitude $|p^\lambda|^2$ of the ultrasound signal. Or, put differently, the h^λ arise from superposition of $h(\xi)$ with weights $|p^\lambda|^2$. If the family $\{p^\lambda\}_{\lambda\in\Lambda}$ is chosen in such a way that the integral transform (2.17) is invertible, then the focused data can be recovered by inversion of an integral transform with kernel $|p^\lambda|^2$.

Not every ultrasound signal can be generated in practice. The choice of possible ultrasound signals is limited by the experimental setup and the characteristics of the transducer. In [30], several types of waves were suggested for synthetic focusing in ultrasound modulated electrical impedance tomography (also called acousto-electric tomography, AET). The measurements in AET depend, at least for small perturbations, linearly on the ultrasound amplitude $|p|$ (see [31]), while in UOT this dependence is quadratic. Thus, it would likely be difficult to create ultrasound signals for which the squared amplitude $|p|^2$ corresponds to a monochromatic or plane wave, which are two of the main examples in [30]. On the other hand, spherical waves, i.e. focusing ultrasound along spheres, also suggested in [30], will be applicable to UOT as well. The measurements then correspond to integrals of the point-focused ultrasound signal over spheres, and focused data can be recovered by inverting spherical mean Radon transform (see [29] for an overview).

2.5.2. Reconstruction from ultrasound localized along lines

One approach to synthetic focusing is based on the observation that in practice narrowly focused ultrasound signals have more resemblance with lines than points (see Figure 2.8, left). If line-shaped ultrasound signals are scanned in linear and angular increments, the resulting measurements correspond to the Radon transform (X-ray transform in 3D) of the data for point-focused ultrasound. Inversion techniques for Radon and X-ray transforms are widely known and well-studied [24, 44]. This approach has been verified experimentally in [37, 38], where direct UOT images were reconstructed by filtered backprojection from measurements with linear and angular scanning of the ultrasound column. In the following section, we will show how this technique can be applied to recover point-focused data from scanning measurements with ultrasound signals focused along lines, which can then be fed to the reconstruction algorithms from Section 2.3.

We assume that the ultrasound beam can be localized along arbitrary lines L intersecting the domain of interest U. Again we restrict our discussion to the 2D case, $U \subset \Omega \subset \mathbb{R}^2$. Lines are parametrized by their normal $\omega \in S^1$ and distance s from the origin, which we choose to be the midpoint of the domain U (see Figure 2.10). Points x on a line L with normal ω and distance s from the origin are characterized by the equation $x \cdot \omega = s$. The set of ultrasound signals is $\{p^L\}_{L\in\Lambda}$ with $\Lambda = \{(\omega, s) : \omega \in S^1, s \in [0, \frac{d}{2}]\}$, where d denotes the diameter of the domain. The signal p^L is a distribution such that $|p^L|^2$ is the Dirac measure of the line L, i.e.

$$\int_\Omega |p^L(x)|^2 f(x)\, dx = \int_L f(x) dx \qquad \text{for all } f \in C^\infty(\Omega).$$

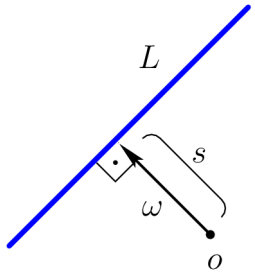

Fig. 2.10. Parametrization of a line L by normal ω and distance s from origin.

Then the measurements for such signals are, according to (2.17), given by

$$\begin{aligned} \hat{h}(\omega, s) = v^L(\eta) &= \int_\Omega h(\xi)|p^L(\xi)|^2 \, d\xi \\ &= \int_{x\cdot\omega=s} h(\xi) \, d\xi. \end{aligned} \tag{2.18}$$

This is the *Radon transform* of the point-focused measurements $h(\xi)$:

$$\hat{h} = \mathcal{R}h. \tag{2.19}$$

A well-known inversion formula for Radon transform is the *filtered backprojection (FBP)* formula [24, 44]:

$$h = \frac{1}{4\pi}\mathcal{R}^{\#} H \frac{d\hat{h}}{ds}. \tag{2.20}$$

Filtered backprojection involves the *backprojection* operator $\mathcal{R}^{\#}$ and the Hilbert transform H. For a function $g : S^1 \times \mathbb{R} \to \mathbb{R}$, the action of these operators is given

by

$$\big(\mathcal{R}^{\#}g\big)(x) = \int_{S^1} g(\omega, \omega \cdot x)\, d\omega,$$
$$\big(Hg\big)(\omega, s) = \text{v.p.} \int_{\mathbb{R}} \frac{g(\omega, \tau)}{s - \tau}\, d\tau.$$

$\mathcal{R}^{\#}$ integrates over all lines passing through x, while $H\frac{d}{ds}$ represents a filter in the variable s. In most numerical implementations of (2.20), the filtration step is applied in FFT domain, and backprojection is computed by quadrature. See [24] for details on the implementation.

2.5.3. Numerical example for ultrasound localized along lines

Here we repeat some of the calculations from Section 2.4 with ultrasound signals localized along lines. To approximate real ultrasound more realistically, signals are not chosen as exact lines but rather have some spread transverse to the line direction. For a line L with parameters (ω, s), the numerical line function we use is given by

$$p^L(x) = \begin{cases} l(x \cdot \omega - s) & \text{if } |x \cdot \omega - s| \leq \delta, \\ 0 & \text{else,} \end{cases}$$

with the line profile

$$l(t) = k\left(\frac{e^{-(\frac{t}{\delta})^2} - e^{-1}}{1 - e^{-1}}\right)^{\frac{1}{2}}.$$

The normalization constant k is chosen such that $\int_{-\delta}^{\delta} l^2(t)\, dt = 1$, and the line half width δ is set to 0.1 in the computations, resulting in ultrasound signals as shown in Figure 2.11. Forward simulations are run as described in Section 2.4.3, with the

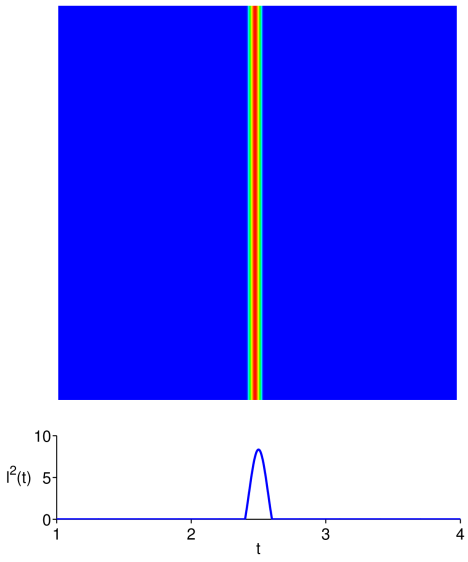

Fig. 2.11. Ultrasound intensity $|p^L|^2$ focused along line with $\omega = \binom{1}{0}$, $s = 0$ (top). Profile in x-direction (bottom).

ultrasound signal scanned in 512 angular and 512 linear increments. The measurements are, as in Section 2.4.3, the values of the modulated light intensities v^L at the detector location $\eta = (5\text{ cm}, 2.5\text{ cm})$.

According to (2.19), inverse Radon transform is applied to the collected measurements $\{v^L(\eta)\}_{L\in\Lambda}$ to recover the measurements $\{v^\xi(\eta)\}_{\xi\in U}$ for point-focused ultrasound signals. FBP is used as the computational algorithm for inverting Radon transform, where the filter is computed in FFT domain and backprojection is calculated by quadrature [24]. Since inversion of Radon transform by itself is ill-conditioned (although only slightly so, see [44]), this procedure is prone to polluting the measurements with high frequency noise that would be amplified by the reconstruction algorithms from Section 2.3. To avoid issues of this kind, an additional low-pass filter

is added to the filtration step of FBP to smoothen the results of Radon inversion. This extra step is common to reduce noise in the computational results of FBP [24].

FBP recovers point-focused measurements $v^{\xi}(\eta)$ on a 50×50 grid of focus points covering the reconstruction domain $U = [1 \text{ cm}, 4 \text{ cm}]^2$. Then, Algorithms 2 and 3 are applied as described in Section 2.4 to reconstruct the absorption coefficient μ_a. The results for the three absorption phantoms from 2.4.2 are shown in Figure 2.12.

Reconstruction quality is almost as good as in the examples in Section 2.4. There is a slight increase in high-frequency noise owing to the concatenation of two modestly ill-posed operations. Also, a gradual decay towards the detector location is visible in the line profile especially for the phantoms with small variation and multiple inclusions. Overall, singularities in the coefficients are well visible with sharp reconstruction of the boundaries, and reconstructed absorption values are close to the correct ones.

In practice, neither the high ultrasound resolution of 512 angular and 512 linear increments nor the uniform focus along lines shown in Figure 2.11 are realistic assumptions. However, the results clearly show that synthetic focusing can be a viable preprocessing procedure for applying the reconstruction process from Section 2.3 to UOT measurements with certain types of non-focused ultrasound signals.

2.6. Stability of the linearized problem

Intuitively, reconstruction in UOT is expected to be substantially more stable than reconstruction from boundary measurements in OT, since ultrasound focusing results in measurements containing localized interior information that is not available

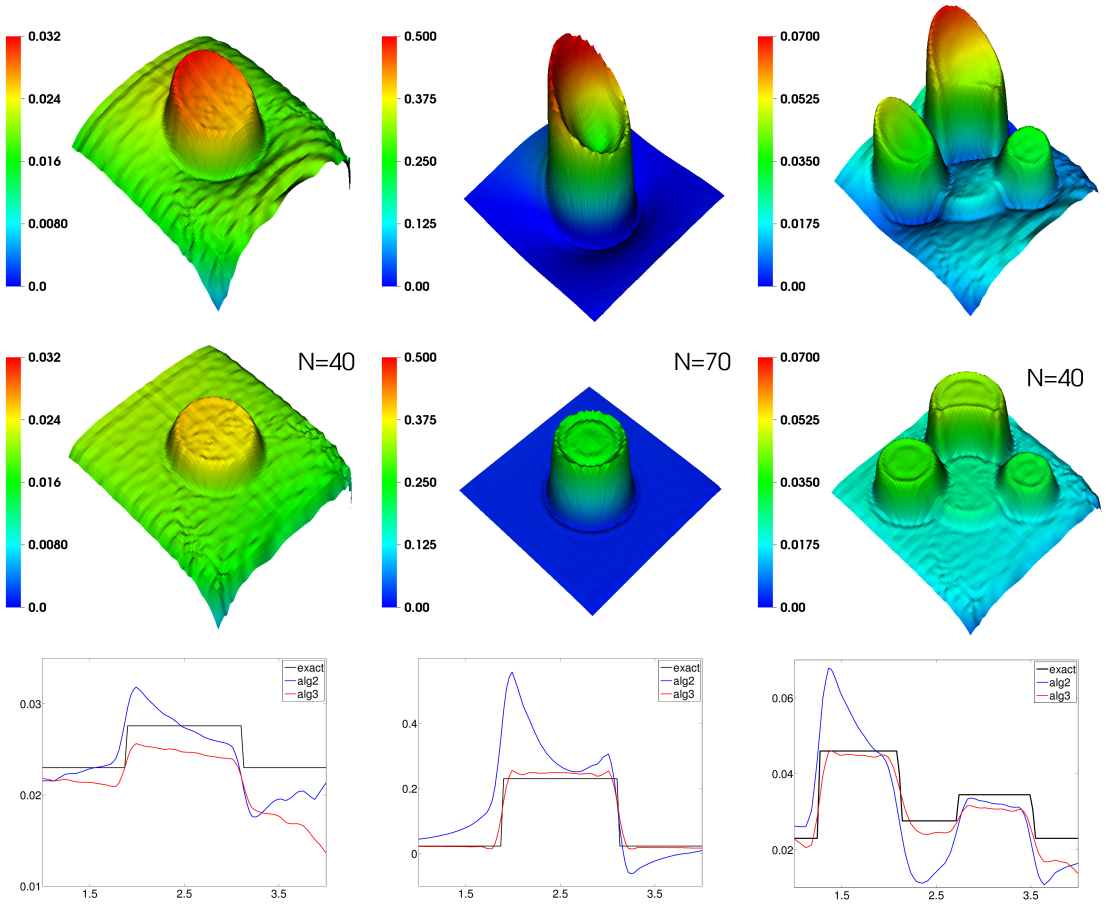

Fig. 2.12. Reconstruction results for the three coefficient phantoms: Algorithm 2 (top), Algorithm 3 after $N = 40, 70$ and 40 iterations (middle), reconstruction profiles along cutlines (bottom, cutlines as in figure 2.7).

from OT measurements. The quality of reconstructions observed in our numerical simulations, especially the recovery of sharp singularities by Algorithm 3, confirms this intuition. In this section, a first step is made towards understanding the stability of reconstruction in UOT.

Note that even though equations (2.9) defining u and v are linear, the relation between absorption coefficient μ_a and measurements h is nonlinear. In this section, we consider a (formal) linearization of the system (2.9) that will allow us to gain some insight into the local properties of the inverse problem.

Let $\Omega \subset \mathbb{R}^d$ with $d = 2$ or $d = 3$ be an open bounded domain with C^2-boundary. We use the notation $\mu := \mu_a$ throughout this section. Let us assume that μ is a small perturbation of a known background absorption $\mu_0 \in C^{0,1}(\overline{\Omega})$ with $\mu_0 > 0$, so that

$$\mu(x) \;=\; \mu_0(x) + \varepsilon\mu_1(x), \qquad \varepsilon \ll 1.$$

We formally write the solutions u and v^ξ to (2.9) as an asymptotic expansion in the small parameter ε:

$$\begin{aligned} u(x) \;&=\; u_0(x) + \varepsilon u_1(x) + o(\varepsilon), \\ v^\xi(x) \;&=\; v_0^\xi(x) + \varepsilon v_1^\xi(x) + o(\varepsilon), \end{aligned} \tag{2.21}$$

Here, $o(\varepsilon)$ denotes terms of higher order in the small parameter ε. Our goal is to relate the first order perturbations of the absorption coefficient μ_1 and the measurements $h_1(\xi) := v_1^\xi(\eta)$, where $\eta \in \partial\Omega$ is the location of the detector.

Let us again assume perfectly focused ultrasound, i.e. $|p^\xi(x)|^2 = \delta(x - \xi)$. By inserting the above expansions into equations (2.9) and sorting terms according to

powers of ε, we get the zeroth order perturbation system

$$-\nabla \cdot D\nabla u_0(x) + \mu_0(x)u_0(x) = 0, \tag{2.22}$$

$$-\nabla \cdot D\nabla v_0^\xi(x) + \mu_0(x)v_0^\xi(x) = \alpha\delta(x-\xi)u_0(x), \tag{2.23}$$

and the first order perturbation system

$$-\nabla \cdot D\nabla u_1(x) + \mu_0(x)u_1(x) = -\mu_1(x)u_0(x), \tag{2.24}$$

$$-\nabla \cdot D\nabla v_1^\xi(x) + \mu_0(x)v_1^\xi(x) = \alpha\delta(x-\xi)u_1(x) - \mu_1(x)v_0^\xi(x) \tag{2.25}$$

for all $x \in \Omega$. These equations are complemented by inhomogeneous Robin boundary conditions as in (2.4) (with sufficiently smooth source term S) for u_0 and homogeneous Robin boundary conditions for v_0^ξ, u_1 and v_1^ξ. Here we neglect the (weak) dependence of D on μ and instead set $D \equiv \text{const} > 0$ for the rest of this section.

Equations (2.22)–(2.23) imply that u_0 and v_0^ξ are solutions to the forward model for absorption coefficient μ_0. Under the stated assumptions, standard elliptic regularity theorems (e.g., [20]) imply $u_0 \in H^3(\Omega)$, and by the Sobolev embedding theorem $u_0 \in C^1(\overline{\Omega})$ [16].

Let us assume that the absorption coefficient is known near the boundary, so that it suffices to consider perturbations μ_1 supported on an open set U with C^2-boundary such that $\overline{U} \subset \Omega$. We assume the data $h_1(\xi)$ to be given for all $\xi \in U$. In what follows, we derive an explicit formula for the dependence of μ_1 on h_1 and then study properties of the corresponding linear operator.

Let us denote by $G_0(x, y)$ Green's function as defined in (2.10) corresponding to the background absorption coefficient μ_0. Equation (2.23) implies that for all $x \in \Omega$

and $\xi \in U$,

$$\begin{aligned} v_0^{\xi}(x) &= \int_{\Omega} \alpha G_0(x,z)\delta(z-\xi)u_0(z)\,dz \\ &= \alpha G_0(x,\xi)u_0(\xi). \end{aligned}$$

From (2.25) we can now deduce that

$$\begin{aligned} v_1^{\xi}(x) &= \int_{\Omega} G_0(x,z)\left[\alpha\delta(z-\xi)u_1(z) - \mu_1(z)v_0^{\xi}(z)\right]\,dz \\ &= \alpha G_0(x,\xi)u_1(\xi) - \alpha u_0(\xi)\int_{\Omega} G_0(x,z)G_0(z,\xi)\mu_1(z)\,dz. \end{aligned}$$

Evaluating at $x = \eta$ and solving for u_1 yields

$$u_1(\xi) \;=\; \frac{h_1(\xi)}{\alpha G_0(\eta,\xi)} + \frac{u_0(\xi)}{G_0(\eta,\xi)}\int_{\Omega} G_0(\eta,z)G_0(z,\xi)\mu_1(z)\,dz.$$

We now use this expression to eliminate u_1 from (2.24). Noting that the differential operators now act on ξ and that

$$\left[-\nabla_{\xi}\cdot D\nabla_{\xi} + \mu_0(\xi)\right]G_0(x,\xi) \;=\; \delta(x-\xi),$$

we get

$$\begin{aligned}
0 &= u_0(\xi)\mu_1(\xi) + [-\nabla_\xi \cdot D\nabla_\xi + \mu_0(\xi)] \left(\frac{h_1(\xi)}{\alpha G_0(\eta,\xi)} \right) \\
&\quad + [-\nabla_\xi \cdot D\nabla_\xi + \mu_0(\xi)] \left(\frac{u_0(\xi)}{G_0(\eta,\xi)} \int_\Omega G_0(\eta,z) G_0(z,\xi) \mu_1(z)\, dz \right) \\
&= u_0(\xi)\mu_1(\xi) + [-\nabla_\xi \cdot D\nabla_\xi + \mu_0(\xi)] \left(\frac{h_1(\xi)}{\alpha G_0(\eta,\xi)} \right) \\
&\quad + \left([-\nabla_\xi \cdot D\nabla_\xi] \left[\frac{u_0(\xi)}{G_0(\eta,\xi)} \right] \right) \int_\Omega G_0(\eta,z) G_0(z,\xi) \mu_1(z)\, dz \\
&\quad - 2D \left[\nabla_\xi \left(\frac{u_0(\xi)}{G_0(\eta,\xi)} \right) \right] \cdot \left[\nabla_\xi \int_\Omega G_0(\eta,z) G_0(z,\xi) \mu_1(z)\, dz \right] \\
&\quad + \frac{u_0(\xi)}{G_0(\eta,\xi)} G_0(\eta,\xi)\mu_1(\xi).
\end{aligned}$$

We will frequently view $G_0(\eta, y)$ as a function of y in the following and hence introduce the notation

$$G_0^\eta(y) := G_0(\eta, y) \quad \text{for } y \in \overline{U}.$$

Note that since $\eta \in \partial\Omega$, G_0^η has no singularities on $\overline{U}$ and hence is a regular solution to (2.22) there. Elliptic regularity and Sobolev embeddings then imply that $G_0^\eta \in C^1(\overline{U})$.

Let us define the following operators acting on functions g defined on U:

$$\big(K_1 g\big)(\xi) := -\frac{1}{2u_0(\xi)} \left([-\nabla_\xi \cdot D\nabla_\xi] \left[\frac{u_0(\xi)}{G_0^\eta(\xi)} \right] \right) \int_U G_0^\eta(z) G_0(z,\xi) g(z)\, dz, \tag{2.26}$$

$$\big(K_2 g\big)(\xi) := \frac{D}{u_0(\xi)} \left[\nabla_\xi \left(\frac{u_0(\xi)}{G_0^\eta(\xi)} \right) \right] \cdot \left[\nabla_\xi \int_U G_0^\eta(z) G_0(z,\xi) g(z)\, dz \right], \tag{2.27}$$

and

$$F := 1 - K_1 - K_2.$$

In terms of these operators, our considerations above imply that μ_1 is a solution to the following linear equation:

$$\big(F\mu_1\big)(\xi) \;=\; -\frac{1}{2u_0(\xi)}\left[-\nabla_\xi \cdot D\nabla_\xi + \mu_0(\xi)\right]\left(\frac{h_1(\xi)}{\alpha G_0^\eta(\xi)}\right). \tag{2.28}$$

In order for the above expressions to be well-defined, we have to make sure that u_0 and G_0^η are bounded away from zero on $\overline{U}$. The following lemma follows immediately from the Hopf Lemma (e.g., [47]):

Lemma 1. *There is a constant $c > 0$ such that $u_0 \geq c$ and $G_0^\eta \geq c$ on $\overline{U}$.*

Next we consider the properties of the integral term involved in K_1 and K_2. The important observation here is the following:

Lemma 2. *The mapping*

$$g \mapsto \int_U G_0(z,\cdot)G_0^\eta(z)g(z)\,dz \tag{2.29}$$

is a bounded linear operator from $L^2(U)$ to $H^2(U)$.

Proof: Let us assume that $g \in L^2(U)$. Since $G_0^\eta \in C(\overline{U})$, multiplication by G_0^η is a bounded linear operator on $L^2(U)$. The following integration against $G_0(z,\cdot)$ results in the solution to the diffusion equation with homogeneous Robin boundary condition and right hand side $G_0^\eta g \in L^2(U)$. Elliptic regularity theory (e.g., [16, 20]) implies that this is a continuous operator from $L^2(U)$ to $H^2(U)$. □

Because of the compact embedding of $H^2(U)$ in $L^2(U)$, the operator defined by (2.29), viewed as a mapping from $L^2(U)$ to $L^2(U)$, is compact. In (2.26), this

operator is multiplied by the factor

$$-\frac{1}{2u_0(\xi)}\left([-\nabla_\xi \cdot D\nabla_\xi]\left[\frac{u_0(\xi)}{G_0^\eta(\xi)}\right]\right). \tag{2.30}$$

The functions $u_0, \nabla u_0, G_0^\eta$ and ∇G_0^η are all bounded on $\overline{U}$ because $u_0, G_0^\eta \in C^1(\overline{U})$. Since u_0 and G_0^η satisfy (2.22), the terms $\nabla \cdot D\nabla u_0$ and $\nabla \cdot D\nabla G_0^\eta$ are bounded on $\overline{U}$ as well, and u_0^{-1} and $(G_0^\eta)^{-1}$ are bounded due to Lemma 1. Consequently, multiplication by (2.30) represents a bounded linear operation on $L^2(U)$, and so K_1 is a compact operator on $L^2(U)$. Similarly, K_2 is a compact operator on $L^2(U)$. This leads us to the main result of this section:

Theorem 3. *$F : L^2(U) \to L^2(U)$ is a Fredholm operator of index zero.*

Thus, the kernel $\mathcal{N}(F)$ of F has finite dimension and the range $\mathcal{R}(F)$ is closed and of finite codimension, equal to the dimension of the kernel. This immediately implies the following result:

Corollary 4. *F as an operator from the quotient space $L^2(U)/\mathcal{N}(F)$ to $\mathcal{R}(F)$ has bounded inverse, and the following norm equivalence holds:*

$$c_1\|Ff\|_{L^2(U)} \;\leq\; \|f\|_{L^2(U)/\mathcal{N}(F)} \;\leq\; c_2\|Ff\|_{L^2(U)}. \tag{2.31}$$

The L^2-norm of the right hand side expression in (2.28) can be estimated in terms of the H^2-norm of the measured perturbation h_1, so that we obtain the following stability result:

Theorem 5. *Under the stated assumptions, there is a constant $C > 0$ such that the*

following relation holds:

$$\|\mu_1\|_{L^2(U)/\mathcal{N}(F)} \;\leq\; C\|h_1\|_{H^2(U)}. \tag{2.32}$$

We conjecture that the kernel $\mathcal{N}(F)$ is in fact trivial, and thus the operator F is invertible. This would imply that μ_1 is uniquely determined by the measured perturbation h_1, and allow us to replace the quotient space norms in (2.31) and (2.32) with the regular L^2 norms. However, we have not been able to prove this result yet.

Smoother norm coercive estimates for the absorption can be obtained if stronger assumptions are made on the unperturbed absorption μ_0 and the domain. For instance, if $\mu_0 \in C^\infty(\Omega)$, $S \in C^\infty(\partial\Omega)$, and Ω has smooth boundary, the operators K_1 and K_2 defined in (2.26)–(2.27), are of order -2 and -1, respectively, in the Sobolev scale:

$$\begin{aligned} K_1 \quad &: \quad H^s(U) \to H^{s+2}(U), \\ K_2 \quad &: \quad H^s(U) \to H^{s+1}(U). \end{aligned}$$

This and the Sobolev embedding theorem [1] imply that for any $s \geq 0$, F is a Fredholm operator on $H^s(U)$, which in turn leads to the estimate

$$\|f\|_{H^s(U)} \;\leq\; c\left(\|f\|_{L^2(U)} + \|Ff\|_{H^s(U)}\right) \tag{2.33}$$

for all $f \in H^s(U)$. Thus, we have the following result:

Theorem 6. *Under the stated assumptions, for any $s > 0$ there is a constant C such that*

$$\|\mu_1\|_{H^s(U)} \;\leq\; C\left(\|\mu_1\|_{L^2(U)} + \|h_1\|_{H^{s+2}(U)}\right).$$

If only a specific value of s is of interest, the smoothness assumptions on μ_0, S and $\partial\Omega$ can be relaxed accordingly.

2.7. Conclusion and outlook

2.7.1. Summary

In this chapter we have introduced a mathematical model for UOT that is based on describing the effect of ultrasound modulation to optical light propagation in the diffusion regime. Under this model, the reconstruction of optical material properties turns into a parameter estimation problem for a coupled set of diffusion equations. A simple reconstruction scheme was introduced for recovering the spatially varying absorption coefficient from boundary measurements of light intensities modulated by point-focused ultrasound signals. Numerical experiments show that under these assumptions stable reconstruction with sharp features and quantitatively correct values of the absorption coefficient is possible. We then discussed the idea of synthetic focusing which, after an additional preprocessing step, allows our reconstruction algorithm to be applied to measurements with certain types of ultrasound signals not focused to individual points. Numerical experiments with ultrasound focused along lines showed results with comparable quality to those obtained with point-focused ultrasound. An initial stability analysis for a linearized version of our model provides some insight as to why reconstruction from measurements with focused ultrasound is only mildly unstable. This corresponds to our observations from the numerical results, which were computed without further stabilization.

2.7.2. Open issues

To verify the practical applicability of our model and the reconstruction scheme, reconstructions should be computed from actual physical measurements instead of using data from numerical simulations. We expect this to be challenging since real-life experiments rarely satisfy the idealized assumptions made in the derivation of our algorithm. However, there is some room for improvement: While we assumed the modulated light intensity to be measured only by a single photon detector, multiple detectors could be placed around the boundary to collect spatially distributed measurement data. This would improve resistance to noise and provide complementary information for reconstruction. However, our current reconstruction scheme would have to be adjusted to deal with this type of measurement data.

It is known that the scattering coefficient also contains information about the physiological state of cells. Hence, it would be interesting to investigate if the measurements available in UOT allow reconstruction of both absorption and scattering at the same time.

More recently it has been observed that the type of internal data available from measurements in UOT follows a more general principle also found in other hybrid imaging modalities [8, 27, 33]. Research efforts are under way to establish a general theoretical framework for analysis of tomography problems with internal data. It can be hoped that such results and the reconstruction schemes arising from them will be applicable to the UOT model presented in this text.

The synthetic focusing approach discussed in Section 2.5 could be extended to other types of ultrasound signals, in particular pressure waves focused along nar-

row spherical wavefronts. The resulting preprocessing step would correspond to reconstruction in thermoacoustic tomography, for which substantial theory and reconstruction algorithms have already been developed [19, 28].

The linearized stability analysis provided in Section 2.6 is still at an early stage. A characterization of the kernel of the Fredholm operator F in (2.28) is missing. It also needs to be shown that the formal linearization we applied is indeed a valid local approximation to the nonlinear problem. Then, the stability result for the linearization could be extended locally to the nonlinear model.

CHAPTER III

DETECTION OF SMALL RADIOACTIVE SOURCES BY 3D BACKPROJECTION

3.1. Introduction

3.1.1. Motivation

Recent security threats have led to a reassessment of scenarios for terrorist attacks. One of the worst case scenarios involves the illicit import or fabrication of a nuclear weapon within the boundaries of the US, which if successfully deployed in a terrorist attack would have disastrous consequences. A major obstacle to the assembly of nuclear weapons is the availability of a critical mass of highly enriched nuclear material. Fissile materials used in nuclear weapons are typically composed of uranium-235 (U-235), uranium-233 (U-233) or plutonium-239 (Pu-239). The production, transport and storage of such substances is tightly regulated and controlled within the US. The enrichment process required for the production of weapon grade nuclear material is highly complex and requires sophisticated technology and equipment, so that the risk of illegal enrichment facilities being operated within the country is deemed small. A more plausible threat is the illicit import of highly enriched material or a nuclear weapon itself. Multiple smaller amounts of subcritical mass could be smuggled along different routes and assembled to a nuclear weapon inside the country.

Of particular concern as a target channel for influx of nuclear material are cargo ports. In 2008, an estimated 14 million cargo containers were handled by all US container ports [57]. Automated facilities have been established for screening incom-

ing cargo for radioactivity, and measures have been implemented to rate the risk of individual cargo containers to contain illicit nuclear material based on origin and contents of containers and the available intelligence information. Due to cost and time limitations, it is currently not possible to thoroughly inspect every single container. However, there is a congressional mandate to improve screening facilities and technology in the near future. Besides cargo ports, similar security issues also arise at airports and land border crossings, as well as for non-cargo maritime transport. There, various types of freight, luggage and vehicles need to be inspected for the presence of nuclear material.

A major issue for screening objects by measuring emitted radioactivity is that highly enriched uranium (HEU) in particular only emits small amounts of radioactivity. A subcritical mass of HEU can be easily shielded by lead containment to further reduce the amount of emitted gamma radiation. The levels of radioactivity emitted from such sources is often not sufficient to be distinguished from the naturally present background radiation. This background stems from atmospheric and cosmic sources, soil and building materials, as well as radiation emitted by legitimate freight like fertilizer, ceramics, or other products containing rock or potassium. Hence, screening for enriched nuclear materials at border controls is a difficult task, and there are severe time constraints for detection devices to obtain and process radiation measurements. In this setting, current detection technology is prone to either generate too many false positives, in which case expensive manual inspection of the containers is required, or false negatives, meaning that objects containing illegal nuclear material may enter the country undetected [18].

Consequently, new detection technology needs to be developed that targets specific properties of the substances that are at risk for smuggling and use in improvised nuclear weapons. In this work, the specific property enabling detection is the small geometric size that illicit nuclear material is expected to have. The critical mass for HEU corresponds to a sphere of diameter between 10 and 20 cm, depending on the degree of enrichment. Concealing larger amounts of weapon grade material would require a substantial quantity of high-Z materials for shielding, which in turn can be detected by radiography [18]. Radiation from a small radioactive source however has a different geometric footprint than background radiation: It originates from a small volume fraction inside the object under investigation, in contrast to natural background radiation being emitted from larger distributed structures.

Some modalities from medical imaging, even though they are generally not suitable for applications with very low signal-to-noise ratios (SNRs), are known to correctly reflect locations of singularities even under missing data conditions. While reconstruction of singularities is usually not sufficient in medical imaging, knowing locations of singularities is enough to reveal small radiating sources. This principle has first been used for detection in [5, 19]. There, backprojection algorithms were applied to collimated and Compton measurements generated from 2D simulations of cargo containers with a small source buried within a strong background signal. A probabilistic analysis of backprojection showed that it has the potential to reveal statistical anomalies in the data that indicate the presence of small localized radiation sources. The purpose of this chapter is to extend the theoretical estimates and computational results of [5, 19] to the practically important case of detection inside

3D volumes.

3.1.2. Types of measurements

Commonly used devices for detecting nuclear material in cargo can be categorized as active or passive modalities. Active detectors irradiate the object of interest with X-ray, gamma or neutron radiation and measure the resulting transmission or reflection signal. Passive detectors measure radiation emitted by the object itself. Since passive detectors do not expose cargo, passengers of vehicles or safety personnel to any harmful radiation, their use in the detection scenarios poses less safety concerns and is easier to handle since no radiation sources need to be operated.

The types of radioactivity emitted from nuclear material include gamma radiation and neutrons. Alpha and beta radiation is readily absorbed by most materials and hence does not play a role in detection. In principle, assuming availability of suitable detectors, the detection method discussed in this text can be applied to both gamma and neutron radiation. Hence, we will jointly refer to both neutrons and photons in the gamma spectrum as "particles" in the following.

Since enriched nuclear material does not necessarily emit a large amount of radiation, measuring radioactivity in terms of particle counts only will usually not siffice for detecting the presence of sources with reasonable certainty. In this text we assume that the locations of particle interactions with sensors are measured as well as certain information about the direction from which particles originated. We distinguish between two cases of directional information that sensors can supply:

- If the direction from which a particle originated is measured by the sensor, we

speak of *collimated* measurements. This type of measurement is most common in medical imaging, particularly in X-ray computed tomography (CT). Sensors that can supply this type of information restrict the field of view of a gamma or neutron detector to a single direction by collimation with thin lead tubes or a mask. Particles that arrive at the sensor with their direction not aligned to collimator direction are absorbed by the collimator and not registered by the sensor. This implies that collimated sensors are unidirectional and are not sensitive to particles from directions other than the collimator direction, which means that a major share of the emitted particles is not recorded by the sensor. Unfortunately, since radiation levels emitted from weak sources are already very low, this low sensitivity renders collimated sensors unsuitable for the purpose of detection. Hence collimated measurements, while often desirable in theory, cannot be obtained with sufficient SNRs in practice.

- In Compton type sensors, particles experience Compton scattering at the sensor, and the location and scattering angle are recorded. This effectively determines a hollow cone of possible directions from which a particle may have originated. For gamma radiation, sensors of this type are known as *Compton cameras* and have been suggested in the 1970s [54]. Neutron sensors based on a different physical principle that provide the same type of data for neutron radiation are currently under development. We will jointly refer to the measurements provided by such sensors as *Compton type* data. While this type of data contains less information than collimated measurements, sensors do not require collimation and hence have a much higher sensitivity, making them

more suitable for detection in practice.

The backprojection based detection scheme suggested in [5, 19] was initially applied to collimated measurements, and a probabilistic explanation was given why the method is successful at detecting small sources. In 2D the two types of measurements are closely related, since a conic surface can be viewed as the union of two half-lines. This allows backprojection algorithms for collimated measurements to be extended to backprojection for Compton type measurements in a relatively straightforward way. In 3D however, the relation between the two types of measurements is more complicated. Nevertheless, backprojection can be viewed as a purely geometrical operation, and this geometric interpretation is readily applicable to Compton data in 3D.

3.1.3. Outline

In Section 3.2, the setup of the detection problem and the different types of measurements are explained in detail. Section 3.3 deals with the connection between the detection problem and a medical imaging modality called *single photon emission computed tomography* (SPECT). The backprojection operator as a common ingredient for reconstruction schemes in SPECT is introduced and its application to the detection problem is discussed. In Section 3.4, the statistical properties of backprojection are analyzed in the setting of the detection problem. For collimated measurements, under certain assumptions on the statistics of background and source formulas are derived for the confidence that a particular set of measurements cannot be explained by the presence of background radiation alone, in which case the pro-

posed detection scheme will claim the presence of a source. Some simple numerical schemes for simulating random background radiation and computing backprojection in 3D by backpropagating individual particles on a discrete grid are discussed in Section 3.5. In Section 3.6, results from Monte Carlo simulation of the background are used to verify the confidence estimates from Section 3.4. Then, synthetic measurements are generated for cargo containing a small source and the suggested backprojection scheme is applied to study feasibility of detection. Section 3.7 concludes with a discussion of the results and an outlook to directions for future research. The methodology used in this text closely follows the ideas presented in [5, 19].

3.2. Setup

A passive detection facility can be realized as a gate that cargo, vehicles or luggage entering the country at border crossings or ports pass through. During the screening process objects remain inside the detector gate for a certain amount of time while measurements of particles emitted from the object are recorded. For each particle that is measured, the detector records location of the particle interaction and collimated or Compton type information about its direction.

3.2.1. Collimated measurements

A 2D schematic of a collimated sensor is shown in Figure 3.1. For each particle that reaches the sensor plate, the location of particle interaction $\mathbf{x}$ and orientation Θ of the collimator is recorded. In a 3D geometry, a planar detector plate with an attached collimator grid is used, so that $\mathbf{x} \in \mathbb{R}^2$ and $\Theta = (\alpha, \varphi)$, where α and φ are

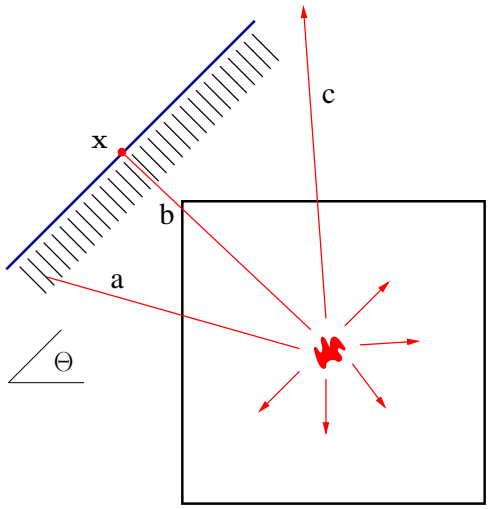

Fig. 3.1. Collimated particle detector. Particle **a** is absorbed by the collimator, particle **b** is recorded with location **x** and direction Θ, particle **c** misses the detector.

elevation and azimuth angle of the collimator.

During the detection process, the sensor is rotated around the object to collect particles from different directions. In 3D, the collected particle data is a four-dimensional set (linear offset from the center of the detector plate, elevation and azimuth of the collimator).

It can be seen from Figure 3.1 that particles with directions not lined up with the collimator will be absorbed and hence not be measured, explaining the low sensitivity of collimated sensors mentioned in the previous section.

3.2.2. Compton measurements

Compton measurements are obtained from devices similar to Compton cameras. Compton cameras were suggested in 1974 [54] for measuring gamma photons. See Figure 3.2 for the principle of Compton cameras. The sensor consists of two layered detection plates. Photons incident on the first plate experience Compton scattering and continue along the scattered direction to the second detector plate, where photons are absorbed. The locations x^0 of scattering and x^1 of absorption are recorded, as well as the energies E_0 of scattering and E_1 of absorption. From the energies the scattering angle ψ is determined by the relation [15, 54]

$$\cos\psi \;=\; 1 - \frac{mc^2 E_1}{(E_1 + E_2)E_2},$$

where c is the speed of light and m is electron mass. On the other hand, ψ and the particle direction d are related to the vector $\beta = x^0 - x^1$ by

$$\cos\psi \;=\; -\frac{\langle d, \beta\rangle}{|d|\,|\beta|}. \tag{3.1}$$

Hence for each detected photon, the scattering angle ψ and the direction $\beta = x^0 - x^1$ determine a hollow cone of possible directions from one of which the photon must have originated. As the vertex of such cones is restricted to the sensor plate, the data is five-dimensional (linear two-dimensional offset on sensor plate, cone central axis β and scattering angle ψ).

Compton detectors have been used in astronomy [2, 50], medical imaging [51, 52, 54] and for monitoring of nuclear sites [48, 49]. The advantages of Compton detectors over collimated detectors are an increased field of view and higher overall

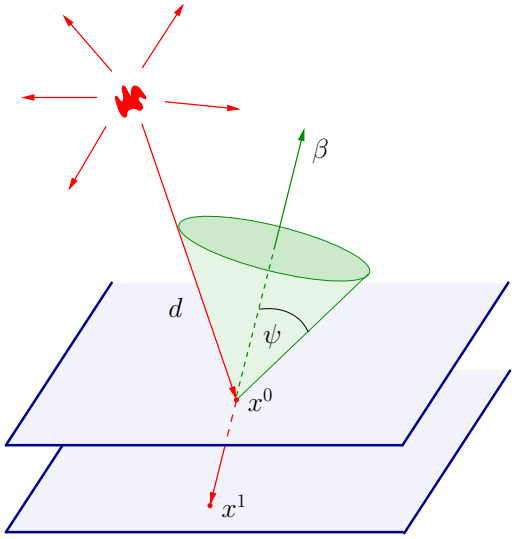

Fig. 3.2. Compton camera detector. Photons are scattered at first detector plate, absorbed at second detector plate.

sensitivity due to lack of collimation. On the other hand, the information obtained from each particle measurement is less specific in comparison to collimated measurements, and the set of measurements has a sparse structure in the five-dimensional data space. This complicates computational discretizations to continuous reconstructions schemes for Compton data. See [46] for an overview of Compton imaging.

Currently, detectors for neutron radiation are being developed based on different physical principles that measure the same type of information as Compton cameras. We will not distinguish between these different physical measuring principles in the following and jointly refer to them as Compton type sensors.

3.2.3. Sources of radiation

A major obstacle to the detection of small radioactive sources is the presence of background radiation. Overall the radiation measured by the sensors originates from three different types of sources:

1. Background from atmospheric and cosmic radiation, natural soil radioactivity and radiation emitted from concrete and other building materials located in the vicinity of the detection device. This signal generally originates from larger structures, and its statistical properties do not change significantly between different screening sessions. Shielding the detection device from this type of radiation is difficult to achieve especially for high energy gamma rays.

2. Natural radiation from legitimate cargo. In particular materials containing rock, soil or potassium like concrete, fertilizer or cat litter naturally emit small amounts of gamma radiation. The contribution from these sources depends on the particular type of cargo. In many cases, larger amounts of cargo of the same type are located in a single container, and the radiation then originates from a larger fraction of the container volume. This type of radiation is frequently the cause of false positives in the detection process.

3. Radiation from illicit nuclear material. Such sources would likely be very weak due to shielding and other measures taken to conceal the material. The amount of nuclear material is expected to be small due to the high efforts involved in acquisition and production. Hence, this type of source can be expected to be geometrically small.

Overall, the signal-to-noise ratio between ballistic particles from illicit sources and the natural background radiation is often as low as 0.1%. The number of particles that is measured by the sensors depends on the radiation intensity of the sources, the sensitivity of the sensors and the time that is spent for acquiring the measurements.

3.3. Relation to medical imaging

3.3.1. SPECT imaging

The situation in detection of small nuclear sources is similar to the one in the medical imaging modality *single photon emission tomography* (SPECT). In SPECT, a radiopharmaceutical combining a gamma emitting isotope with biomarkers is injected into a patient's bloodstream, where the biomarkers cause the radioisotope to attach to sites of physiological interest. Photons emitted by the radioisotope are detected by collimated detectors and an image of the isotope distribution inside the patient is reconstructed by a computational reconstruction algorithm. The image can provide information about the functional state of organs or other sites that the biomarkers attached to. The main differences to the setting in detection of small radioactive sources are:

- Even though radioisotopes used in SPECT are only weakly radioactive, the signal-to-noise ratio is typically much higher than what is expected for detection of nuclear sources.

- In SPECT, the characteristics of the radioisotope are known and the acquisition times are longer (15-20 minutes) than acceptable sojourn time for container

screening (<1 minute).

- While in SPECT an actual image of the radioisotope distribution needs to be reconstructed, this is not necessary for detection of nuclear sources. A strong indication that a cargo container contains unusual radioactive sources is sufficient for deciding to assign the container to a thorough inspection procedure.

In SPECT, reconstruction of images under the low SNRs expected in the detection problem would be considered impossible. However, since imaging is not necessary for detection of nuclear sources, there is still hope that reliable detection schemes can be devised even for low SNRs. In [5, 19] it was shown that backprojection, an operation that is a common ingredient for many tomographic reconstruction algorithms, yields promising results for detection of small nuclear sources. In the following we discuss the definition of backprojection for collimated data in 3D. We largely follow the presentation in [44, 45].

3.3.2. Backprojection for collimated measurements

Let $\Omega \subset \mathbb{R}^3$ be the domain covered by the object under investigation. Collimated particle measurements for given collimator angle and a given offset on the planar sensor can be interpreted as superposition of particles originating from a fixed line. Let $\theta \in S^2$ denote the normalized collimator direction and $x \in \theta^\perp$ the offset on the sensor plane. In terms of elevation α and azimuth φ of the collimator, $\theta \in S^2$ is

given by

$$\theta = \begin{pmatrix} \cos\varphi\cos\alpha \\ \sin\varphi\cos\alpha \\ \sin\alpha \end{pmatrix}.$$

We assume that radiation is isotropic, i.e. particles are equally likely to be emitted in each direction, and there is no scattering of particles. Let $f(y)$ be the source intensity and $\mu(y)$ the attenuation at $y \in \Omega$. Then for a sufficiently large number of detected particles, the expected value of the particle count is given by the line integral

$$\big(P_\mu f\big)(\theta, x) \;=\; \int_{-\infty}^{\infty} f(x+t\theta) e^{-\int_t^\infty \mu(x+\tau\theta)\,d\tau}\,dt. \tag{3.2}$$

P_μ is called the *attenuated X-ray transform* (or *attenuated ray transform*) operator. It maps the function f to weighted integrals over straight lines parametrized by $\theta \in S^2$ and $x \in \theta^\perp$. $P_\mu f$ is a function on the set $T = \{(\theta, x) : \theta \in S^2, x \in \theta^\perp\}$.

The problem in SPECT is to recover f from measurements of $P_\mu f$. This problem is often aggravated by the fact that the attenuation map μ is unknown and only partial measurements of $P_\mu f$ are available. To simplify the discussion, let us assume that $\mu = 0$ and $P_\mu f$ is given on all of T. In this case $P := P_0$ is simply integration of f along lines:

$$\big(Pf\big)(\theta, x) \;=\; \int_{-\infty}^{\infty} f(x+t\theta)\,dt. \tag{3.3}$$

An operator that is frequently useful for reconstruction is the *backprojection* operator, which for a function g on T is given by

$$\big(P^\# g\big)(y) \;=\; \int_{S^2} g(\theta, E_\theta y)\,d\theta \qquad \text{for all } y \in \mathbb{R}^3. \tag{3.4}$$

Here, $E_\theta y = y - (y \cdot \theta)\theta$ is the orthogonal projection of y onto $\theta^\perp$, see Figure 3.3. $P^\#$ can be interpreted as the geometric dual of P: While P integrates functions along lines, $P^\#$ at a point y integrates line data over all lines passing through y.

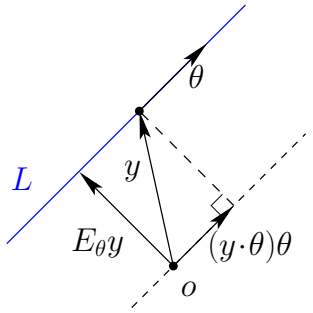

Fig. 3.3. Orthogonal projection $E_\theta y$ for line L.

Also we have

$$\begin{aligned}\int_{S^2}\int_{\theta^\perp} g(\theta,x)\big(Pf\big)(\theta,x)\,dx\,d\theta &= \int_{S^2}\int_{\theta^\perp} g(\theta,x)\int_{-\infty}^{\infty} f(x+t\theta)\,dt\,dx\,d\theta\\ &= \int_{S^2}\int_{\mathbb{R}^3} g\Big(\theta, y-(y\cdot\theta)\theta\Big) f(y)\,dy\,d\theta\\ &= \int_{\mathbb{R}^3} \big(P^\# g\big)(y)\, f(y)\,dy.\end{aligned}$$

Hence, $P^\#$ is the adjoint operator of P.

A well-known reconstruction formula for recovering f from Pf is the so-called *filtered backprojection* (FBP). It says that for $g = Pf$, under some mild assumptions (see [45] for details) we have

$$f = \frac{1}{(4\pi)^2} P^\# I g, \tag{3.5}$$

where I denotes the Riesz potential operator of order -1 on T, which is defined by its Fourier transform:

$$\widehat{(I\,g)}\,(\theta,\xi) = |\xi|\,\widehat{g}(\theta,\xi), \quad \xi \in \theta^{\perp}.$$

Here $\widehat{\ }$ denotes Fourier transform in the variable $x \in \theta^{\perp}$. I acts as a filter that amplifies high frequencies, which explains the term *filtered backprojection* for the operator in (3.5).

Since complete knowledge of $(Pf)(\theta,x)$ for all $(\theta,x) \in T$ is rarely available in practice, it has been noted that FBP is not as useful for reconstructions in 3D SPECT as it is in 2D [45]. However, FBP schemes are very well studied, and it is known that FBP correctly reconstructs singularities in the intensity distribution even for missing data and unknown attenuation. For example, if $\mu \in C_0^{\infty}(\Omega)$ is an unknown attenuation coefficient, the results from [32] imply that under quite general assumptions the function

$$\frac{1}{(4\pi)^2} P^{\#} I P_{\mu} f$$

has singularities at the same locations as f. In medical imaging, singularities often express boundaries between different types of tissue, and small inclusions in tissue can indicate malign cell mutations. It is remarkable that filtered backprojection can reconstruct the locations of such inclusions without knowledge of the attenuation map μ.

For the detection of radioactive material, small sources represent singularities in the radiation intensity map, while background radiation from larger structures is more smooth and evenly distributed. This observation was used in [5, 19] to show

that even though there is a large background present in the detection problem, FBP can still reliably detect the presence of small sources. It was also discovered there that the filtration operator in FBP is not useful for detection, since it further amplifies the dominating background noise in the signal. Backprojection by itself was found to be more reliable under strong background noise than FBP.

A heuristic explanation for the usefulness of backprojection for detecting small sources can be given as follows: Let us assume for a moment that inside Ω there is only a single point source located at $p \in \Omega$, so that f is a Dirac delta function centered at p. Then all collimated measurements for lines that do not cross p will be zero. The backprojection of the measurements at each point different from p will only involve few lines with non-zero measurements, while the backprojection at p will include all lines with non-zero measurements. Hence, we expect the backprojected image to have a sharp peak at p. Even if there is a strong but spread out background superimposed on f during the measurements, this would lead to a rather smooth distribution in the backprojected image, from which the sharp peak at p may still be distinguishable. In the following section, a statistical interpretation will yield some estimates that show under which assumptions backprojection can successfully detect small sources.

The discussion of backprojection techniques so far has been limited to collimated measurements. The theory for reconstruction from Compton data is far less developed and only few reconstruction formulas are available [15, 19, 55]. The analytical meaning of backprojection in this case is not well understood in 3D. Still, the geometric interpretation of backprojection as an averaging process over all geometric

primitives intersecting a given point, can be easily carried over to Compton type measurements.

In the following section, we will restrict our attention to collimated measurements and derive some probabilistic estimates that show the usefulness of backprojection for detection. We will return to Compton type data in Section 3.6.3, where some numerical simulations for detection by backprojection of Compton measurements will be presented.

3.4. Probabilistic estimates for backprojection of collimated measurements

In this section, we follow the probabilistic approach taken in [5, 19] to develop an understanding of why and when backprojection can be useful for detecting geometrically small sources. To this end we try to formalize the intuition given in the previous section: If there is a small radiating source present inside the scanned object, then backprojection of collimated measurements should peak near the location of the source. See Figure 3.4 for an illustration of this idea. By investigating the statistical properties of the data from collimated measurements, we will be able to estimate under which conditions such a peak will be pronounced enough to be distinguished from the background.

3.4.1. Confidence estimates

In the detection problem, the signal is quite weak and measurements consist of individual particle counts per line. Hence, instead of integrating measurements over all directions as the backprojection formula (3.4) implies, we sum the number of particle

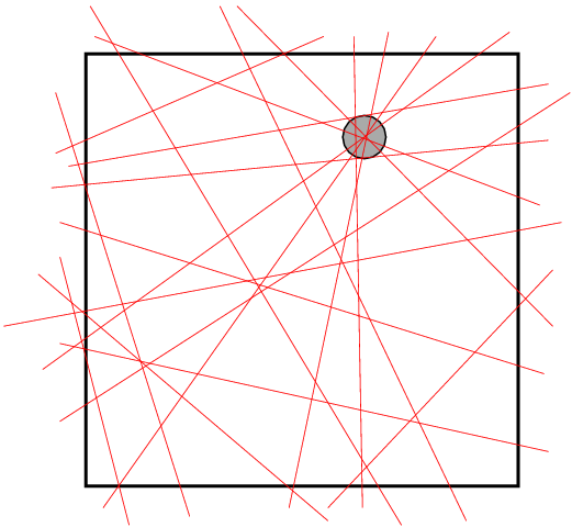

Fig. 3.4. Accumulation of particle trajectories near a source.

trajectories intersecting a small volume centered at $x \in \Omega$ and use this count as our approximate backprojection value at x. We will frequently call this process of counting lines intersecting a certain volume *backpropagation* in the following to distinguish from backprojection as defined by formula (3.4). If this count is significantly higher in a certain region than what we would expect from the background radiation, we claim that there is a source located there.

First, let us estimate what contribution the background radiation will have in this process. To simplify this discussion, let us assume that trajectories of background particles are uniformly distributed random lines intersecting Ω. This means that the average local density of particle trajectories is constant throughout Ω. Such particle trajectories would result from a uniform distribution of background sources over the whole space that emit uniformly in all directions. This assumption may not be

exactly true in practice, for example background particles emitted from legitimate mildly radioactive cargo necessarily originate from the interior of Ω. However, since the background radiation in general originates from larger, distributed structures, we expect the assumption of uniformly distributed trajectories of background particles to be reasonable. See [26] and the discussion in Section 3.5.1 for more details about the definition of uniform randomness for geometric objects.

What is the probability for a random line to intersect a small volume inside Ω? Let us consider a cube C_R of linear size R and a smaller cube C_r of linear size $r \ll R$ contained in C_R. According to [26], the probability p of a random line intersecting C_R to also intersect C_r is given by the ratio of the surface areas of C_r and C_R:

$$p = \frac{\int_{\partial C_r} dS}{\int_{\partial C_R} dS} = \frac{6r^2}{6R^2} = \frac{r^2}{R^2}. \tag{3.6}$$

For N independent random lines intersecting C_R, the probability that i of the lines also intersect C_r is described by the binomial distribution $B(N, p)$ and is given by $\binom{N}{i} p^i (1-p)^{N-i}$.

Suppose the object to be scanned for sources is a cube of linear dimension R, and let us subdivide this domain into $N_{\text{vox}} := (R/r)^3$ smaller cubic voxels of linear size $r \ll R$. This setup is depicted in Figure 3.5. The value of r should correspond approximately to the dimension of a small source that we try to detect. In practice, the ratio r/R is expected to be around 0.01, with R on the order of several meters and r several centimeters.

Let X be a random variable describing the number of lines intersecting a given voxel. If only the uniformly distributed background is present, then X is distributed

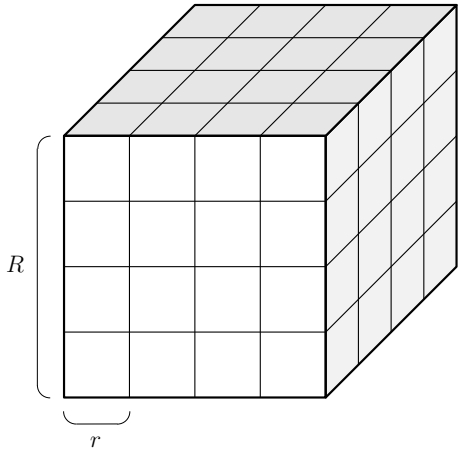

Fig. 3.5. 3D grid of voxels of size r.

according to the binomial distribution $B(N, p)$. However, if the count of lines intersecting the given voxel is very far in the tail of the distribution $B(N, p)$, then such an event is unlikely to be explained only by the presence of the background. To measure how far in the tail the line count is, we will calculate the distance from the mean $\mu := Np$ of the binomial distribution in terms of its standard deviation $\sigma := \sqrt{Np(1-p)}$. If this distance is significantly large in a voxel, we claim that there is a source located there. Let k be a fixed threshold such that the probability of the random variable X to exceed $\mu + k\sigma$ is very small. This probability is given by the cumulative distribution function (cdf) of the binomial distribution:

$$P_k := P(X > \mu + k\sigma) = 1 - P(X \leq \mu + k\sigma) = 1 - \sum_{i=0}^{\lfloor \mu + k\sigma \rfloor} \binom{N}{i} p^i (1-p)^{N-i}. \quad (3.7)$$

Here, $\lfloor \cdot \rfloor$ denotes the floor function.

If more than $\mu + k\sigma$ lines intersect a single voxel, the detection scheme indicates

the presence a source. The confidence that such an accumulation of lines is not due to the random background is given by $1 - P_k$. We have to take into account that this accumulation can happen in any of the N_{vox} voxels. If we assume that the random variables X for different voxels are independent, the probabilities of no more than $\mu + k\sigma$ lines intersecting in any of the voxels due to the random background is

$$c_k := \prod_{i=1}^{N_{\text{vox}}} (1 - P_k) = (1 - P_k)^{N_{\text{vox}}} = \left[\sum_{i=0}^{\lfloor \mu + k\sigma \rfloor} \binom{N}{i} p^i (1-p)^{N-i} \right]^{N_{\text{vox}}}. \tag{3.8}$$

Under our assumptions, c_k is also the confidence that an accumulation of more than $\mu + k\sigma$ lines in at least one voxel is not due to the random background.

In reality, the random variables X are not truly independent between different voxels. If a voxel is intersected by a particular line, the probability that this line also intersects a neighboring voxel is higher than the probability that it intersects a voxel far away. However, this conditional dependence is difficult to quantify. We will show results from computational simulations below that indicate that the error introduced by neglecting this dependence is in fact small.

Now let us assume that there is a source of size r present inside the screened object. We can use equations (3.6)–(3.8) to determine under which circumstances the source will be successfully detected by backpropagation. Assume that we have a rough estimate of the SNR s, such that the number of particles measured will be $N + n_s$ with N background particles and $n_s := sN$ particles originating from the source. Our goal is to estimate how big N should be to reliably detect the source. The particle measurements will be backpropagated on a grid of $N_{\text{vox}} := (R/r)^3$ voxels. The source will not be lined up with the voxel grid, but there will be a voxel from

which at least $n_s/8 = sN/8$ source particles originate. The random background will contribute about Np particles to each voxel. Thus the source will be detected by the backpropagation scheme if

$$sN/8 + Np \;>\; \mu + k\sigma = Np + k\sqrt{Np(1-p)}.$$

This is equivalent to

$$N \;>\; 64\left(\frac{k}{s}\right)^2 p(1-p). \tag{3.9}$$

Hence for a fixed value of k the source can always be detected if N is chosen large enough. Unfortunately, the confidence level c_k in (3.8) depends on both k and N, so that a fixed value of k does not correspond to a fixed confidence level.

From (3.9) we find that $k \approx \frac{s}{8}\left(\frac{N}{p(1-p)}\right)^{1/2}$, and using this in (3.8) yields the confidence level depending on N only:

$$c \;\approx\; \left[\sum_{i=0}^{\lfloor (p+s/8)N \rfloor} \binom{N}{i} p^i (1-p)^{N-i}\right]^{N_{\text{vox}}}. \tag{3.10}$$

Now for a desired confidence level, we can choose N such that the right hand side of (3.10) is larger than the confidence level, and this value of N provides an estimate of how many particles need to be measured in order to detect the source.

Let us look at an example: We would like to detect a source of approximate diameter $r = 10$ cm with an SNR of $\sim$0.1% inside a container of size $R = 10$ m with a confidence of at least 99%. Thus $s = 10^{-3}$ and $p = (r/R)^2 = 10^{-4}$. From (3.10), we find that for $N = 2.75 \times 10^5$ the confidence is[1] $c \approx 0.99$, and this corresponds to a

[1]To evaluate the binomial cdf the routine `binocdf` from the MATLAB Statistics Toolbox [53] was used.

value of $k \approx 6.6$. Hence, we should measure approximately 275,000 particles. After backpropagating these measurements on a grid of $N_{\text{vox}} = (R/r)^3 = 10^6$ voxels, if any of the voxels have more than $\mu + k\sigma \approx 62$ lines intersecting, we can claim with at least 99% confidence that this cannot be explained by the random background only.

3.4.2. Approximations to the binomial distribution

The cdf for the binomial distribution is difficult to evaluate when the number of Bernoulli trials is large. The representation using the binomial coefficient in (3.8) is not practical for values of N that are common in the detection problem. For large number of trials, the binomial distribution is often approximated by simpler probability distributions that are easier to handle. In the following, two very common approximations are discussed, the normal and Poisson approximations. In Section 3.6.1, the resulting confidence estimates are verified using Monte Carlo simulations.

Normal approximation. For large N and values of p not too close to 0 or 1, the binomial $B(N, p)$ is well approximated by the normal distribution $\mathcal{N}(\mu^{\mathcal{N}}, \sigma^{\mathcal{N}})$ with mean $\mu^{\mathcal{N}} = Np$ and standard deviation $\sigma^{\mathcal{N}} = \sqrt{Np(1-p)}$. Various rules of thumb have been suggested in the literature to determine for which exact range of N and p the normal approximation is valid (see [34] for an overview). Most of these rules imply that the normal approximation should be valid in the detection setting, however they generally focus on the probabilities resulting from the approximation, rather than derived quantities like the cdf that is of interest here. The normal approximation has been successfully used for estimating confidences of detection in 2D in [5, 19].

Approximating the number of background lines intersecting a particular voxel by a normal random variable $X^{\mathcal{N}} \sim \mathcal{N}(\mu^{\mathcal{N}}, \sigma^{\mathcal{N}})$, the probability of more than $\mu^{\mathcal{N}} + k\sigma^{\mathcal{N}}$ lines intersecting is

$$P_k^{\mathcal{N}} := P(X^{\mathcal{N}} > \mu^{\mathcal{N}} + k\sigma^{\mathcal{N}}) \;=\; \frac{1}{\sigma^{\mathcal{N}}\sqrt{2\pi}} \int_{\mu^{\mathcal{N}}+k\sigma^{\mathcal{N}}}^{\infty} e^{-\frac{(x-\mu^{\mathcal{N}})^2}{2(\sigma^{\mathcal{N}})^2}}\, dx = \frac{1}{2}\operatorname{erfc}\left(\frac{k}{\sqrt{2}}\right),$$

where $\operatorname{erfc}(x) = \frac{2}{\sqrt{\pi}} \int_x^{\infty} e^{-t^2} dt$ is the complementary error function.

If independence of the random variable $X^{\mathcal{N}}$ across different voxels is assumed, the confidence that a line count exceeding $\mu^{\mathcal{N}} + k\sigma^{\mathcal{N}}$ in any of the voxels is not due to the random background is

$$c_k^{\mathcal{N}} = \left[1 - \frac{1}{2}\operatorname{erfc}\left(\frac{k}{\sqrt{2}}\right)\right]^{N_{\text{vox}}}. \tag{3.11}$$

Poisson approximation. For large values of N and small values of p, $B(N,p)$ is accurately represented by the Poisson distribution $\text{Pois}(\lambda)$ with $\lambda = Np$. Mean and standard deviation of this discrete probability distribution are given by $\mu^{\mathcal{P}} = \lambda = Np$ and $\sigma^{\mathcal{P}} = \sqrt{\lambda} = \sqrt{Np}$. The Poisson distribution is frequently used to model radioactive decay [56], which is the underlying process for generating the radiation that is observed in detection.

The probability for a Poisson distributed random variable $X^P \sim \text{Pois}(\lambda)$ to attain values exceeding $\mu^{\mathcal{P}} + k\sigma^{\mathcal{P}}$ is given by

$$P_k^{\mathcal{P}} := P(X^{\mathcal{P}} > \mu^{\mathcal{P}} + k\sigma^{\mathcal{P}}) \;=\; \sum_{j>\mu^{\mathcal{P}}+k\sigma^{\mathcal{P}}} e^{-\mu^{\mathcal{P}}} \frac{(\mu^{\mathcal{P}})^j}{j!} \;=\; 1 - \frac{\Gamma(\lfloor \mu^{\mathcal{P}} + k\sigma^{\mathcal{P}} + 1 \rfloor, \mu^{\mathcal{P}})}{\lfloor \mu^{\mathcal{P}} + k\sigma^{\mathcal{P}} \rfloor !},$$

where $\Gamma(s,x) = \int_x^{\infty} t^{s-1} e^{-t} dt$ is the upper incomplete gamma function.

Assuming independence between voxels, the confidence that line counts above

$\mu^{\mathcal{P}} + k\sigma^{\mathcal{P}}$ are not stemming from the background is

$$c_k^{\mathcal{P}} = \left[\frac{\Gamma(\lfloor \mu^{\mathcal{P}} + k\sigma^{\mathcal{P}} + 1 \rfloor, \mu^{\mathcal{P}})}{\lfloor \mu^{\mathcal{P}} + k\sigma^{\mathcal{P}} \rfloor !} \right]^{N_{\text{vox}}} . \tag{3.12}$$

3.5. Computational methods

In order to test the effectivity of the backprojection detection scheme numerically, we simulate the measurement process and apply backprojection to the resulting synthetic measurements. In this section, algorithms for simulating the random background and computing backprojection will be discussed. The algorithms will subsequently be used in Section 3.6 to verify the confidence estimates given in Section 3.4 and numerically simulate 3D detection of small sources. There are three main tasks for which computational schemes are introduced in the following:

- Simulation of the background radiation.
- Backprojection of collimated measurements.
- Backprojection of Compton measurements.

Throughout this section, the computational domain is chosen as the 3D cube $\Omega = [-1, 1]^3$.

3.5.1. Simulating random background radiation

For simulation purposes the background radiation will be modeled as a sample of random lines intersecting the detection domain Ω. There is some inherent ambiguity attached to the meaning of randomness of geometric objects, see for example the

detailed discussion of Bertrand's paradox in [23]. In essence, there are many ways of interpreting geometric randomness, and there is no natural reason for picking one interpretation over another, unless additional information about the desired kind of randomness is given. The point of view taken in this text is that a random distribution of lines ought to be invariant under rotations and translations, and this determines the distribution uniquely [26]. Note that this assumption had already been used implicitly in (3.6). Another way to think of this invariance is that the local density of lines from a random sample should be uniform throughout Ω.

There are some pitfalls associated with picking random lines in 3D. For example, one might expect that random lines in Ω could be generated by picking a random starting point from Ω and a direction uniformly random from S^2. But in fact this choice of parametrization neglects lines originating outside Ω that still intersect Ω due to their direction. Since these missing lines have a higher chance of intersecting the corner regions of Ω, lines sampled according to this rule have a higher density near the center of Ω. Probability densities for parametrizations of lines that lead to a uniform distribution have been given in [12]. We use the *chord model* for which it was shown e.g. in [39] that it produces uniformly distributed lines. According to the chord model, random lines can be generated as follows:

Algorithm 1.

1. *Pick two independent random points uniformly distributed on a sphere encompassing* Ω.
2. *Connect the points to form a line.*
3. *Discard lines that do not intersect* Ω.

Since $\Omega = [-1,1]^3$, we take the sphere to be of radius $\sqrt{3}$ centered at the origin. To choose points uniformly distributed on this sphere, following [63] we pick u uniformly from $[-1,1]$, θ uniformly from $[0,2\pi)$ and set

$$x = \sqrt{3-3u^2}\cos\theta, \qquad y = \sqrt{3-3u^2}\sin\theta, \qquad z = \sqrt{3}u.$$

Hence, to generate a random line, four random numbers need to be drawn, and the probability of rejecting a line for not intersecting Ω is $1-2/\pi \approx 0.36$. If Algorithm 1 is implemented on a regular desktop computer and efficient random number generators are used, millions of random lines can be generated within a few seconds.

3.5.2. Backprojection of collimated measurements

Collimated particle measurements consist of a set $\{l_i\}_{i=1}^N$ of N lines that intersect the domain Ω. To backproject these measurements, the integral over the unit sphere in (3.4) needs to be computed. Since in the detection problem the integrand is not a continuous function on S^2 but rather a discrete count of lines, instead of approximating the integral by quadrature we resort to the backpropagation scheme suggested in Section 3.4: The domain is decomposed into smaller cells and for each cell, the number of intersecting lines is computed. This will approximate the integral in (3.4) up to a constant scaling factor.

As in Section 3.4, we decompose the domain Ω into a mesh of n^3 regular cubic voxels of linear size $r = 2/n$. The computational task then is to find for each line l_i the voxels that are intersected by the line, see Figure 3.6. This problem bears some similarity to rasterization of lines in computer graphics [17], which is however more

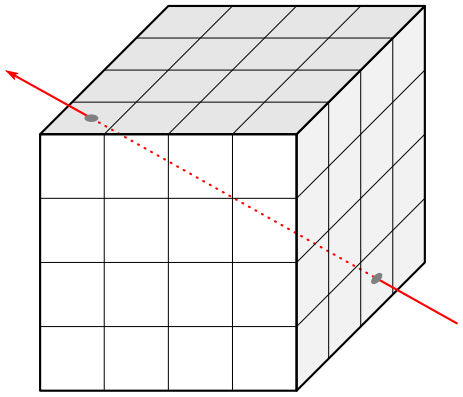

Fig. 3.6. Line intersecting Ω.

common in a 2D setting. Note that a line intersects a given voxel if and only if it intersects one of the voxels' sides. Hence, we can first find the points where a line intersects the grid planes, and then each voxel adjacent to such an intersection point is crossed by the line. This procedure is subsumed in the following algorithm.

Algorithm 2 (Backpropagation of lines)**.**
For each line l_i:

1. *Find the intersections of the line with the grid planes.*
2. *For each voxel that contains at least one of the intersection points, increase its line count variable by one.*

See Figures 3.7–3.8 for an illustration of this algorithm. The number of operations for backpropagating a single line is of order $\mathcal{O}(n)$, and the number of operations for all N lines is of order $\mathcal{O}(Nn)$. Since the backpropagation of individual lines is independent, Algorithm 2 can be easily implemented in parallel. Moreover, particles

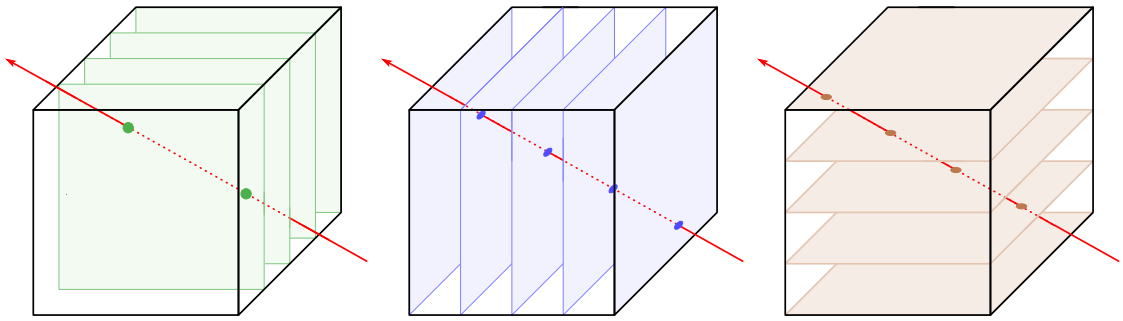

Fig. 3.7. Intersections with grid planes.

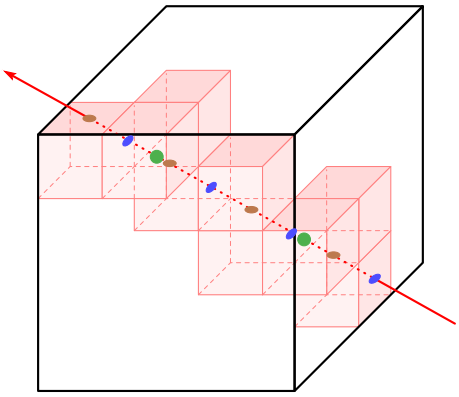

Fig. 3.8. Intersected voxels.

can be backpropagated as soon as they are measured, even while the data collection process is still ongoing.

3.5.3. Backprojection of Compton measurements

For Compton sensors, the measurements consist of a set of hollow cones $\{(x_i^0, \beta_i, \psi_i)\}_{i=1}^N$ given by their vertex x_i^0, central axis β_i and opening half angle ψ_i (see Figure 3.2).

Compton measurements in 2D can be related to collimated measurements and a backprojection formula analogous to (3.4) can be found for the Compton transform [5, 19]. In 3D however, a simple relation between X-ray and Compton transform is not available, and the formal description of a backprojection operator as the adjoint to the Compton transform is not known. Still the geometric interpretation of backprojection as an averaging process over all geometric primitives passing through a fixed point can be readily applied to Compton measurements. For the purpose of computations, we will again resort to a simpler backpropagation scheme: Subdividing the computational domain Ω into smaller cells, we count the number of cone surfaces passing through each cell.

Note that this is really the simplest possible way of backpropagating cone surfaces. It may be beneficial if, instead of merely counting the number of cones intersecting a cell, the contribution of each cone surface is weighted according to the surface area of its intersection with the cell. However, such schemes would likely be more computationally expensive, and should be backed by theoretical justifications of the cone weights. Hence, we leave the investigation of such schemes to future work.

For the subdivision into cells the same regular voxel grid as in Section 3.5.2 is used, see Figure 3.5. While it is possible to determine exactly which voxels a given cone intersects, this is a tedious task. Instead, we choose a small step size $h < r$ and cover the cone surface with a mesh of points approximately distance h apart from each other. Then, we determine for each mesh point the voxel it is contained in.

The meshing strategy for the cone surfaces differs between acute ($\psi \leq \pi/4$) and

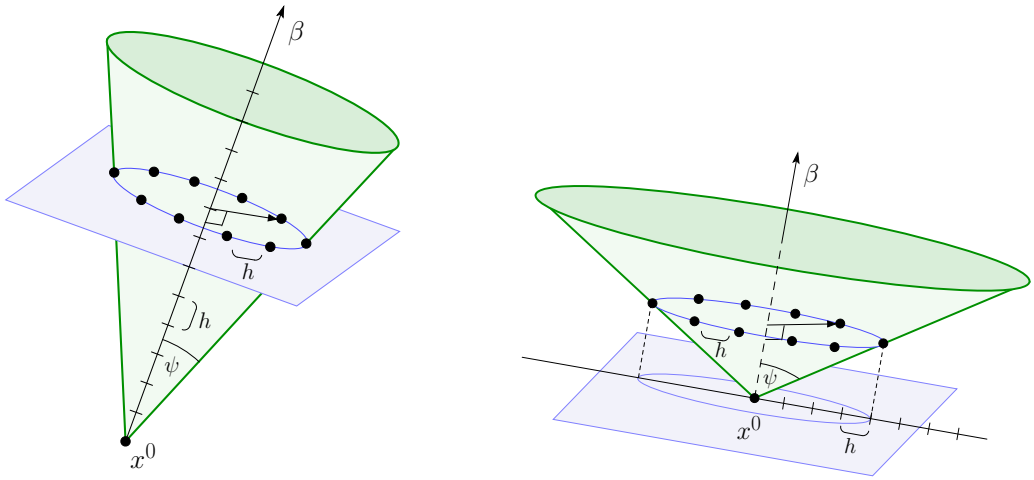

Fig. 3.9. Discrete grid points on conic surface with vertex x^0, central axis β and opening half angle ψ. Acute cone (left), obtuse cone (right).

obtuse ($\psi > \pi/4$) cones: For acute cones, the central axis β is discretized in steps of size h, and at each discrete point, the normal plane to β passing through the point is intersected with the cone surface, resulting in a circle. Then, the circle is discretized in steps of size h. For obtuse cones, the cone surface is intersected with hollow cylinders around the cone central axis with radius kh, $k = 1, 2, ..$, and the resulting circles are discretized in steps of size h. See Figure 3.9 for an illustration of this discretization. We summarize the procedure in the following algorithm.

Algorithm 3 (Backpropagation of conic surfaces)**.**

Choose a step size $h < r$. For each cone, do the following:

1a. If the cone is acute, for $k = 1, 2, \ldots$ intersect the cone surface with planes normal to β through the points $x^0 + kh\beta$.

1b. If the cone is obtuse, for $k = 1, 2, \ldots$ intersect the cone surface with cylindrical

surfaces of axis $x^0 + t\beta$ and radius kh.

2. *Place discrete points spaced at arc length h apart on the resulting circles.*
3. *For each voxel that contains at least one of the discrete points, increase its line count variable by one.*

There is no guarantee that this algorithm finds all voxels which are intersected by a given cone surface. In practice however, for h small enough (e.g. $h = r/2$), the number of voxels missed is very small. Figure 3.10 shows an example of a backpropagated cone surface for different values of h on a grid with $n = 50$ for the cone given by $x^0 = (0, 0, -1)$, $\beta = (0, 0, 1)$ and $\psi = 45°$. The number of operations necessary for backpropagating a single cone is of the order $\mathcal{O}(n^2)$, and for all N cones the operation count is of order $\mathcal{O}(n^2 N)$. Even though this operation count is substantially higher than for backpropagation of collimated data, we note that backpropagation of different cones is independent and hence can be carried out in parallel.

3.6. Simulation results

In this section, Algorithms 1–3 are used to simulate the detection process computationally. In the fist part, the accuracy of the probabilistic estimates derived in Section 3.4 is tested by comparing estimated confidences to the results of a Monte Carlo simulation of the background radiation. In the second part, synthetic collimated measurements from a cargo container containing a small source are generated. Backprojection is applied to the synthetic measurements to investigate the feasibil-

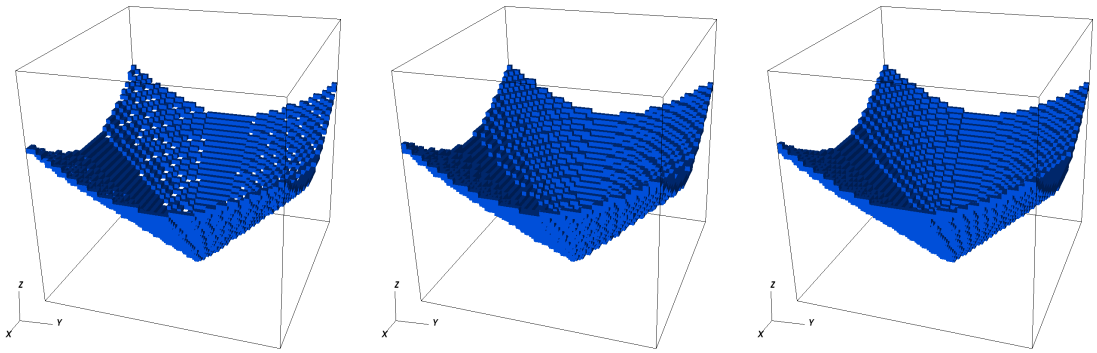

Fig. 3.10. Backpropagated cone surface for $h = r$ (left), $h = 2r/3$ (middle), $h = r/2$ (right).

ity of detection. In the third part, synthetic Compton measurements are generated numerically and Compton backprojection is applied.

3.6.1. Monte Carlo simulation of the background

The confidence estimates given in Section 3.4 were derived under certain assumptions. Independence of the events "a voxel is intersected by a given line" across different voxels was assumed, and in Section 3.4.2, the binomial distribution was approximated by normal and Poisson distributions. To verify that the errors introduced by these approximations are not too large, we simulate a large number of random samples of the background and compare the statistics across the samples to the theoretical estimates.

To this end, we simulate M independent samples of random backgrounds. In each sample, N independent, uniformly distributed lines intersecting $\Omega = [-1, 1]^3$ are generated using Algorithm 1. The lines are backpropagated on a grid of n^3 voxels

to count the number of lines intersecting each voxel. For each sample, the maximum voxel line count is recorded. We set r_k to be the ratio of samples in which the maximal line count does not exceed $\mu + k\sigma$, where μ and σ are mean and standard deviation of the random variables as defined in Section 3.4. We then compare for varying value of k the ratio r_k to the confidence estimate (3.8) from the binomial distribution and the normal and Poisson approximations given by (3.11) and (3.12) respectively.

In the calculations, $M = 10{,}000$ samples are generated with $N = 500{,}000$ random lines each. The lines are backpropagated to a mesh of 100^3 voxels, which corresponds to values $p = 10^{-4}$, $\mu = Np = 50$, and $\sigma = \sqrt{Np(1-p)} \approx 7.07$. Since both the binomial and the Poisson distribution are discrete, their cdf only depends on the integer part of $\mu + k\sigma$. Hence, instead of varying k directly, we vary $\mu + k\sigma$ in integer increments. The corresponding values of r_k, c_k, $c_k^{\mathcal{N}}$ and $c_k^{\mathcal{P}}$ are recorded in Table 3.1. The cdf for binomial and Poisson distribution is evaluated by the routines `binocdf` and `poisscdf` from the MATLAB Statistics Toolbox [53].

It can be seen that for all values of k the binomial and Poisson estimates of the confidence are very close to the rates from the Monte Carlo simulation. The values of the normal estimate on the other hand significantly overestimate the confidence. Consequently, we conclude that normal approximation should be avoided for estimating detection probabilities in 3D, while estimates from the original binomial distribution and the Poisson approximation are generally accurate. For the detection examples in the following section, we will use the Poisson estimate $c_k^{\mathcal{P}}$ to assess confidences of detection.

Table 3.1. Comparison between estimated confidences and statistics from 10,000 samples for different values of k.

k	$\mu + k\sigma$	r_k	c_k	$c_k^{\mathcal{N}}$	$c_k^{\mathcal{P}}$
4.81	84	0.016	0.016	0.468	0.016
4.95	85	0.092	0.093	0.690	0.093
5.09	86	0.258	0.261	0.837	0.260
5.23	87	0.470	0.471	0.920	0.470
5.37	88	0.658	0.659	0.962	0.658
5.52	89	0.797	0.795	0.983	0.795
5.66	90	0.885	0.883	0.992	0.883
5.80	91	0.936	0.935	0.997	0.935
5.94	92	0.966	0.965	0.999	0.965
6.08	93	0.983	0.982	0.999	0.981
6.22	94	0.991	0.990	1.0	0.990

3.6.2. Detection from collimated measurements

We simulate the actual detection process by generating synthetic measurements from a cargo container containing a small source and applying the backprojection detection scheme to the measurements. The detection domain is again the cube $\Omega = [-1, 1]^3$, with a spherical source of diameter 0.02 located at position $(0.1, 0.2, 0.3)$ (we deliberately choose an off-center location in order to avoid symmetries). The background radiation consists of N_b random lines intersecting Ω that are generated using Algorithm 1. The source emits $N_s \ll N_b$ particles that are chosen as random lines intersecting the volume occupied by the source. At the boundary, an array of 100×100 square particle sensors is placed on each side of the cube that measure particle interactions and directions particles originated from. As the location of a particle

interaction the midpoint of the corresponding sensor midpoint is recorded, while directions are measured exactly (up to numerical precision). This generates a set of synthetic measurements $\{l_i\}_{i=1}^{N_b+N_s}$. The setting is a simplification of the scanning measurement process outlined in Section 3.2.1, where sensors needed to be rotated around the object of interest to collect measurements. Also, a more realistic model of the measurements would take into account the limited angular resolution of sensors, as well as measurement errors.

We then apply the backprojection scheme described in Algorithm 2 to backpropagate the measurements on a grid of 100^3 regular cube-shaped voxels. This results in a count of the number of intersecting lines for each voxel. For the first set of results, we choose $N_b = 275{,}000$ and $N_s = 275$ corresponding to our benchmark SNR of 0.1%. According to the example given at the end of Section 3.4 based on estimate (3.10), this setting should allow detection of the source with at least 99% confidence. Mean and standard deviation of the background are $\mu = Np = 27.5$ and $\sigma = \sqrt{Np(1-p)} \approx 5.24$.

The top panel of Figure 3.11 shows a histogram of the voxels according to their particle counts. While most voxels have values around the mean 27.5, there is a small number of voxels to the far right with counts between 120 and 160. To make these outliers more visible in the plot, the bottom panel of Figure 3.11 shows a log histogram of the voxel particle counts. The outliers to the far right are more than ten times the standard deviation away from the mean of the background. According to the Poisson confidence estimates (3.12), the probability of such outliers happening due to the random background is practically zero. Hence, the detection scheme would

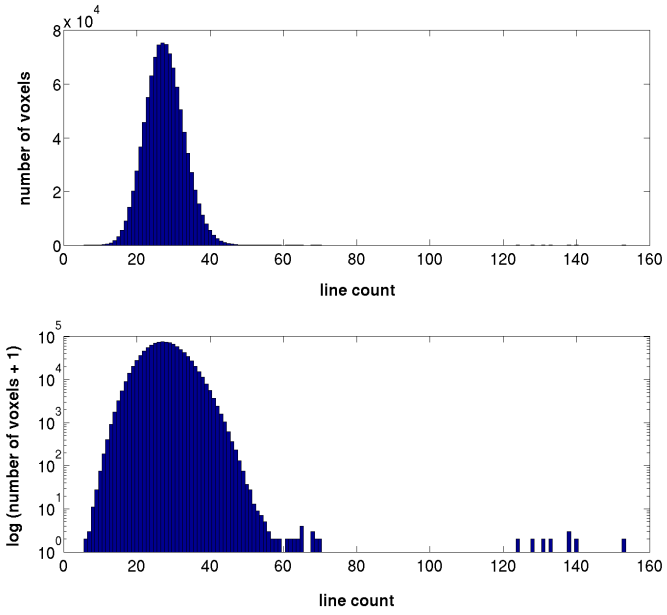

Fig. 3.11. Histogram of voxel particle counts (top), log histogram of voxel particle counts, incremented by one (bottom).

mark this container as suspicious of containing a source.

To verify that the outliers in the histogram are indeed due to the hidden source, a 3D plot of the voxels with line counts exceeding 60 is shown in Figure 3.12. It can be clearly seen that all voxels with line counts above 60 are close to the source location $(0.1, 0.2, 0.3)$.

In the next experiment, we reduce the number of detected background particles to $N_b = 100{,}000$, and the number of source particles to $N_s = 100$, keeping the SNR constant at 0.1%. Mean and standard deviation of the background are $\mu = Np = 10$ and $\sigma = \sqrt{Np(1-p)} \approx 3.16$. Figure 3.13 shows the line counts along the plane $x = 0.1$ that passes through the source. The location of the source is clearly visible.

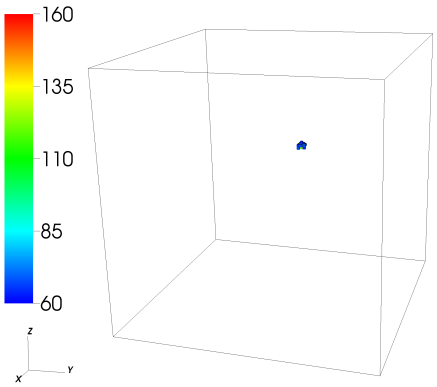

Fig. 3.12. Voxels with line count exceeding 60.

The maximum line count in this case is 58, which is again more than ten standard deviations away from the mean, and the probability that this could happen due to the random background is essentially equal to zero.

Now we investigate how well the detection scheme works for even lower SNR. Figure 3.14 shows the line counts along the same slice $x = 0.1$ for $N_b = 100{,}000$ and $N_s = 40$, corresponding to an SNR of 0.04%. The source is much harder to locate in these images. Indeed, using our Poisson confidence estimate (3.12), we find the confidence for a maximum line count of 28 to be $c_k^{\mathcal{P}} \approx 0.47$. This tells us that such a maximum is actually quite likely to happen due to the random background, and we cannot claim the presence of a source with reasonable certainty.

Next we test what influence the size of the source has on the detection results. With $N_b = 100{,}000$ and $N_s = 100$, we increase the diameter of the source to 0.08, leaving its location unchanged. Intuitively the larger size should increase the number of voxels covered by the source, and hence decrease the average particle count for

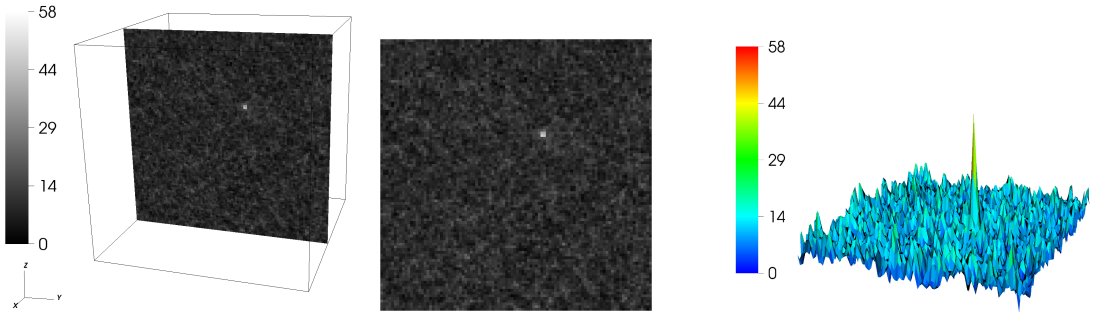

Fig. 3.13. Backpropagation image along the plane $x = 0.1$. Alignment of the plane inside Ω (left), 2D projection (middle), elevated surface plot (right).

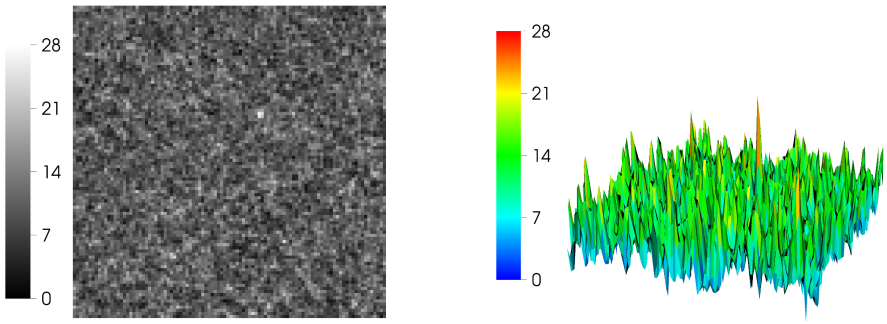

Fig. 3.14. Backpropagation image along $x = 0.1$ for $N_s = 40$. 2D projection (left), elevated surface plot (right).

each such voxel. Figure 3.15 shows the resulting particle counts along the slice $x = 0.1$. Even though the source is barely visible, the maximum line count is 31, corresponding to a detection confidence $c_k^{\mathcal{P}} \approx 0.98$. Note that since the source is now larger than a single voxel, the slice $x = 0.1$ may not contain the voxel of maximum intersection count. This explains why the source is less visible in Figure 3.15 than in, say, Figure 3.14, for which we found a lower detection confidence.

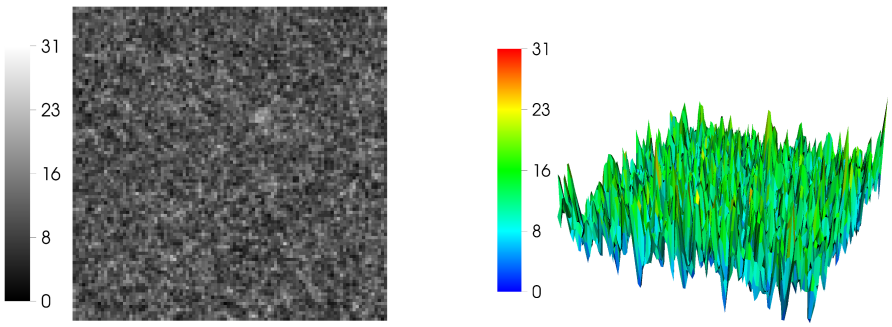

Fig. 3.15. Backpropagation image along $x = 0.1$ for increased source diameter. 2D projection (left), elevated surface plot (right).

In practice, the object to be inspected cannot usually be surrounded by sensors on all sides. Instead, the detection facility is more likely to resemble a gate with sensor arrays on at most four sides of the cargo. To imitate this setting, we remove the particle sensors on the sides given by $y = -1$ and $y = 1$, so that particles that exit Ω through these sides are not registered. In the simulation, random particles keep being generated until $N_b = 100{,}000$ background and $N_s = 100$ source particles are recorded by the remaining sensors. The source diameter is 0.02 and its location is unchanged. Figure 3.16 shows the $x = 0.1$ slice of the backpropagated measurements. The maximum intersection count is 37, and the corresponding confidence is estimated to be practically equal to one. From Figure 3.16, it can be seen that the missing sensors lead to an overall non-uniform distribution of the intersection counts, with on average less particles intersecting voxels close to the missing sensors at $y = -1$ and $y = 1$. In [5, 19], non-uniform background was dealt with by considering deviations from local means over subgrids of pixels. While this technique could be applied in 3D as well, we shall not discuss this in the present text.

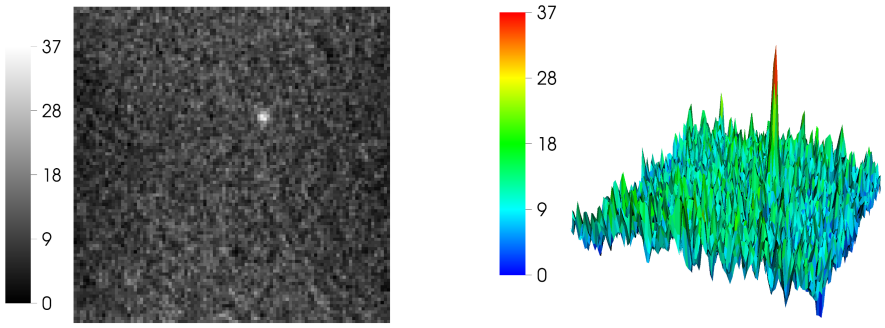

Fig. 3.16. Backpropagation image along $x = 0.1$ for missing sensors in y-direction (horizontal direction in figure). 2D projection (left), elevated surface plot (right).

3.6.3. Detection from Compton type measurements

To simulate detection from Compton-type measurements, we proceed in a very similar way as for detection from collimated measurements. The cone surfaces corresponding to the particle measurements are backpropagated on a grid using Algorithm 3 and superimposed to generate the backprojection image.

During the measurement process, Compton scattering of particles at the sensor plate needs to be simulated in order to choose the half opening angle ψ of the resulting cones (see Figure 3.2). The distribution of Compton scattering angles is given by the Klein-Nishina formula [55]. It depends on the energy of incoming particles, about which we have made no specific assumptions. Hence, to keep the discussion simple, we will assume a uniform distribution of scattering angles instead. Thus, for each particle, at the site of interaction with the sensor the cone central axis β (see Figure 3.2) is chosen from a uniform distribution on the half sphere of directions

pointing away from the sensor plate. The cone half opening angle ψ is calculated using (3.1).

For the computations the same setting as in 3.6.2 is used. The domain Ω is the cube $[-1,1]^3$, and a spherical source of diameter 0.02 is placed at $(0.1, 0.2, 0.3)$. Algorithm 1 generates N_b random lines intersecting Ω and N_s random lines intersecting the source. At the boundary, an array of 100×100 square sensors on each side of Ω records particle hits and randomly generates the central cone axes β from the half sphere of unit vectors pointing away from the sensor plate. As location of the particle interaction the sensor midpoint is recorded, while β and ψ are stored up to numerical accuracy.

The backprojection scheme for Compton data given in Algorithm 3 is applied to backpropagate the measurements on a regular grid of 100^3 cubic voxels. The result is a count of the number of intersecting cone surfaces for each voxel. To visualize these results, we plot the backpropagation values along slices through the source location. Additionally, we show a 3D image of the voxels with values at least 95% of the maximum value. This will serve as a visual indication of how well the source voxels are distinguishable from the background, since we do not have any confidence estimates available for detection from Compton measurements.

In the first example, $N_b = 500{,}000$ background and $N_s = 1{,}000$ source particles are generated, corresponding to an SNR of 0.2%. The resulting intersection counts per voxel range from 3,523 to 6,870. Figure 3.17 shows the values along the slice $x = 0.1$ in the left and middle panel, and the voxels with values exceeding 95% of 6,870 in the right panel. It can be seen that the background radiation leads to a

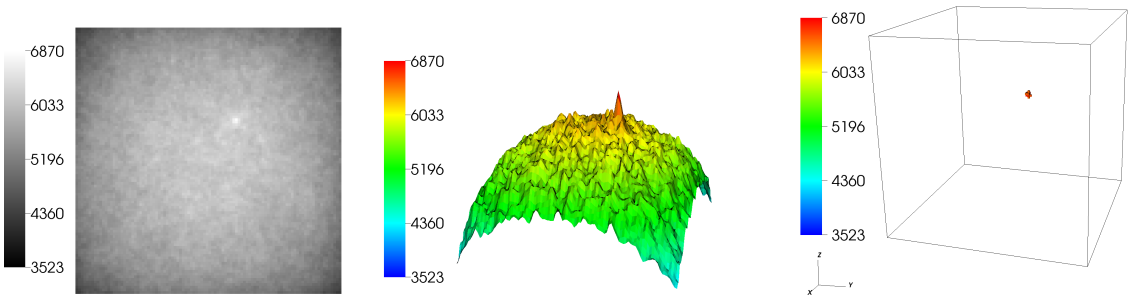

Fig. 3.17. Backpropagation image from Compton measurements. 2D projection (left) and elevated surface plot (middle) along slice $x = 0.1$, voxels with values exceeding 95% of the maximum (right).

non-uniform distribution of the backprojection values. Voxels near the center of the domain are more likely to be intersected by the random cone surfaces than voxels close to the corners of the domain. Still, the location of the source is visible as a peak slightly exceeding the background distribution, and all voxels with values in excess of 95% of the maximum are located at the source location.

We lower the SNR to the benchmark value of 0.1% by setting $N_s = 500$, and the results are shown in Figure 3.18. The source is now very difficult to locate in the image along $x = 0.1$ slice. In the 3D plot, we see that many voxels far from the source have values close to the maximum, making the source nearly indistinguishable from the background. We can no longer claim successful detection in this case.

Next, the diameter of the source in increased to 0.04 and 0.08, while keeping $N_b = 500{,}000$ and $N_s = 1{,}000$. The results are shown in Figures 3.19 and 3.20. While the source of diameter 0.04 is clearly visible, the one of diameter 0.08 cannot be easily distinguished from the background.

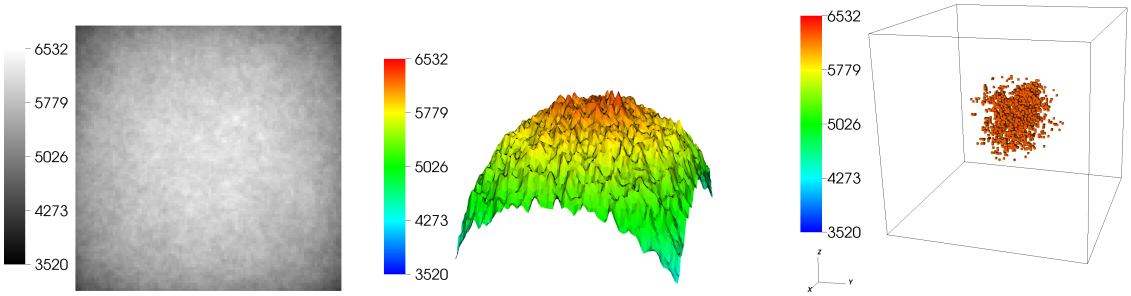

Fig. 3.18. Backpropagation image for $N_s = 500$. 2D projection (left) and elevated surface plot (middle) along slice $x = 0.1$, voxels with values exceeding 95% of the maximum (right).

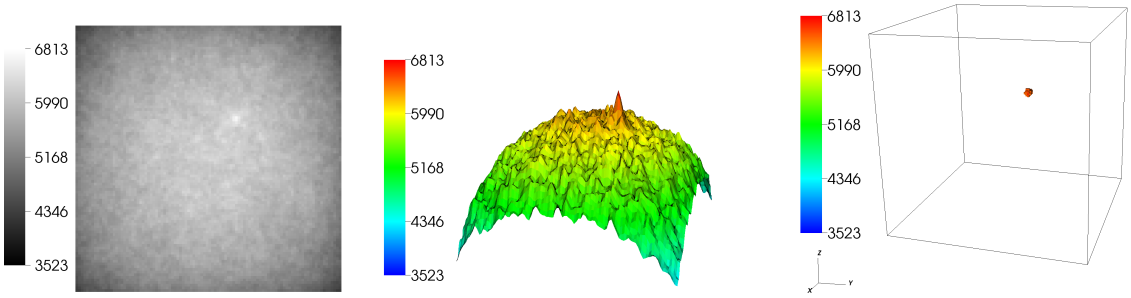

Fig. 3.19. Backpropagation image for source diameter 0.04. 2D projection (left) and elevated surface plot (middle) along slice $x = 0.1$, voxels with values exceeding 95% of the maximum (right).

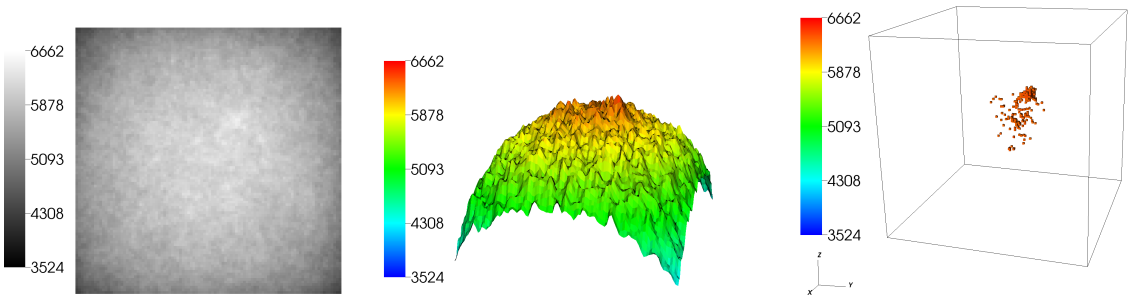

Fig. 3.20. Backpropagation image for source diameter 0.08. 2D projection (left) and elevated surface plot (middle) along slice $x = 0.1$, voxels with values exceeding 95% of the maximum (right).

Finally, we remove the sensor arrays on the sides given by $y = -1$ and $y = 1$. Still, $N_b = 500{,}000$, $N_s = 1{,}000$ and the source has diameter 0.02. Figure 3.21 shows the backprojected image. The shape of the background changed in a similar way as in the collimated case, with on average less cones intersecting the voxels near the missing detectors. Still, the source can be distinguished from the background nearly as well as if sensors were available on all sides.

3.7. Conclusion and outlook

We have demonstrated how backprojection in 3D can be useful in the detection of small nuclear sources. Detection is based on the fact that the signal emitted from geometrically small sources has a characteristic structure in the collected dataset that is emphasized by backprojection. For collimated particle measurements, statistical estimates were given that show under which conditions the signal from a small source can be distinguished from the stronger but more random background. The validity

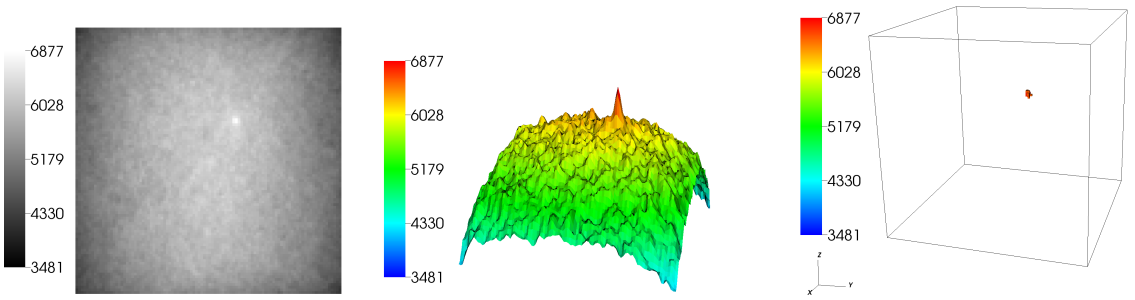

Fig. 3.21. Backpropagation image for missing sensor on $y = -1$ and $y = 1$ sides. 2D projection (left) and elevated surface plot (middle) along slice $x = 0.1$, voxels with values exceeding 95% of the maximum (right).

of the estimates was verified by comparing to statistics from Monte Carlo simulations of random background radiation. A simple grid backpropagation algorithm for computing backprojection of collimated measurements was discussed that allows fast calculation of backprojection images. These can then be analyzed for presence of a source by visual inspection or using the statistical estimates. Confidence estimates derived for collimated measurements allow for automated detection by thresholding of the backprojected measurements. Computational examples of detection from synthetic collimated measurements show the detectability of small sources even for low SNR. Size of the source, SNR, overall number of particles and placement of sensors all influence the feasibility and results of detection by backprojection. For Compton measurements, which are more useful in practice due to increased sensitivity and field of view of the sensors, a theoretical or statistical explanation for the usefulness of backprojection is not available. We applied a simple backpropagation algorithm to backproject Compton data, and its potential for detection of small radioactive

sources was shown in the computational results.

All theoretical and computational results were based on the assumption that the background radiation can be well approximated by a uniformly random distribution of particle trajectories. In practice, the background originates from natural sources and legitimate cargo material that may not be uniformly distributed inside the container, and scattering and absorption contributes to the structure of the background. Hence, it needs to be verified how well the assumption of uniform randomness of the background fits to the practical situation. In the nuclear engineering community, Monte Carlo simulations of containers filled with different materials have been used for testing detection methods [18]. We propose to apply our backprojection scheme to data generated in this way to verify how sensitive our results are to the assumption of a uniform background.

Also, we have not taken into account the effect of limited angular resolution of the sensors. The ability of backprojection to resolve the small size of potential sources crucially depends on the resolution of sensors, and the influence of this factor on detection results needs to be studied.

The backpropagation of Compton measurements led to a non-uniformly distributed background in the backprojected image that makes it harder to detect sources located closer to the center of the domain. It should be investigated if a weight factor can be introduced in the backpropagation of cone measurements in order to remove the non-uniformity of the background.

Lastly, statistical estimates for detection confidences were presented only for the case of collimated measurements. It would be helpful if similar estimates could be

found for the statistics of Compton measurements. This would also provide some insight into how to handle the non-uniform background in Compton backprojection mentioned above.

CHAPTER IV

CONCLUSION

In the first part of this dissertation a mathematical model for ultrasound modulated optical tomography was presented that includes optical properties of the medium, ultrasound modulation and the measurement process. Three simple reconstruction schemes were introduced that can recover the medium's absorption coefficient from scanning UOT measurements with perfectly focused ultrasound waves. We presented numerical reconstructions from synthetic measurements generated for three different absorption phantoms. Reconstructions showed high resolution images with quantitatively correct values of optical absorption. We discussed synthetic focusing techniques in UOT that allow for reconstructions from measurements with certain types of non-focused ultrasound waves. As an example, reconstructions were computed from measurements with ultrasound waves localized along lines. An initial stability analysis for a linearized version of our model is given that explains the stability observed in the numerical reconstruction examples.

In the second part, backprojection schemes in 3D were presented for detecting small nuclear sources inside cargo containers and other objects. We considered two different types of passive detectors that collect collimated or Compton-type data respectively of the radiation emitted from the screened objects. A computational backprojection scheme was suggested that backpropagates trajectories of measured particles on a regular rectangular grid and counts the number of trajectories intersecting each grid cell. For the case of collimated measurements, we estimated the

confidence that measurements are not consistent with the signal expected from a uniformly random background. If this confidence is large, the proposed detection scheme will claim the presence of a radioactive source inside the screened object. We verified the derived estimate computationally using a Monte Carlo simulation of random backgrounds. Synthetic measurements were created for cargo containers containing a small source by sampling from a background distribution and a localized source distribution. The proposed backprojection scheme was applied to the synthetic measurements to assess the feasibility of detection. We found that under our assumption of a uniform background, we were able to detect small sources with SNR as low as 0.1% from collimated measurements. For Compton type measurements, we successfully detected the source for SNR around 0.2%, but found that the proposed backprojection scheme produces non-uniform background images that complicate detection of sources located in corners of the screened object.

REFERENCES

[1] R. A. Adams, *Sobolev Spaces*, Academic Press, New York, 1975.

[2] F. Ait-Ouamer, A.D. Kerrick, A. Sarmouk, T.J. O'Neill, W.E. Sweeney, O.T. Tumer, A.D. Zych, and R.S. White, *Calibration and performance of the UCR double Compton gamma ray telescope*, IEEE Transactions on Nuclear Science, 37 (1990), pp. 535–540.

[3] M. Allmaras, *The step-29 tutorial program of deal.II*, available online at http://www.dealii.org/developer/doxygen/deal.II/step_29.html, 2007.

[4] M. Allmaras and W. Bangerth, *Reconstructions in ultrasound modulated optical tomography*, Journal of Inverse and Ill-Posed Problems, to appear; preprint available at http://arxiv.org/abs/0910.2748, 2011.

[5] M. Allmaras, D. Darrow, Y. Hristova, G. Kanschat, and P. Kuchment, *Detecting small low emission radiating sources*, submitted; preprint available at http://arxiv.org/abs/1012.3373, 2011.

[6] G. B. Arfken and H. J. Weber, *Mathematical Methods for Physicists*, 6th ed., Elsevier Academic Press, Burlington, MA, 2005.

[7] S. R. Arridge, *Optical tomography in medical imaging*, Inverse Problems, 15 (1999), R41.

[8] G. Bal, *Hybrid inverse problems and internal information*, submitted; preprint available at http://www.columbia.edu/~gb2030/PAPERS/IO-Review-Hybrid-11.pdf, 2011.

[9] G. Bal and J. C. Schotland, *Inverse scattering and acousto-optic imaging*, Physical Review Letters, 104 (2010), 043902.

[10] W. Bangerth, R. Hartmann, and G. Kanschat, *deal.II – a general purpose object oriented finite element library*, ACM Transactions on Mathematical Software, 33 (2007), 24/1–24/27.

[11] W. Bangerth, R. Hartmann, and G. Kanschat, *deal.II differential equations analysis library, technical reference*, http://www.dealii.org, 2009.

[12] A. L. D. Beckers and A. W. M. Smeulders, *The probability of a random straight line in two and three dimensions*, Pattern Recognition Letters, 11 (1990), pp. 233–240.

[13] S. C. Brenner and R. L. Scott, *The Mathematical Theory of Finite Elements*, 2nd ed., Springer, Berlin, 2002.

[14] B. Chance, C. Cooper, D. T. Delpy, and E. O. R. Reynolds, *Near infrared spectroscopy and imaging of living systems*, Philosophical Transactions of the Royal Society B, 352 (1997), pp. 643–761.

[15] M. J. Cree and P. J. Bones, *Towards direct reconstruction from a gamma camera based on Compton scattering*, IEEE Transactions on Medical Imaging, 13 (1994), pp. 398–407.

[16] L. C. Evans, *Partial Differential Equations*, American Mathematical Society, Providence, RI, 1998.

[17] J. D. Foley, A. van Dam, S. K. Feiner, J. F. Hughes, and J. E. Turner, *Computer Graphics: Principles and Practice*, 2nd ed., Addison-Wesley Professional, Reading, MA, 1996.

[18] G. Gaukler, C. Li, R. Cannaday, S. Chirayath, and Y. Ding, *Detecting nuclear materials smuggling: Using radiography to improve container inspection policies*, Annals of Operations Research, 187 (2011), pp. 65–87.

[19] Yulia Georgieva-Hristova, *Mathematical Problems of Thermoacoustic and Compton Camera Imaging*, PhD dissertation, Texas A&M University, 2010.

[20] D. Gilbarg and N. S. Trudinger, *Elliptic Partial Differential Equations of Second Order*, Springer, Berlin, 2001.

[21] G. T. Herman, *Fundamentals of Computerized Tomography: Image Reconstruction from Projections*, 2nd ed., Springer, Dordrecht, 2009.

[22] H. E. Hernandez-Figueroa, M. Zamboni-Rached, and E. Recami (Editors), *Localized Waves*, John Wiley & Sons Inc., Hoboken, NJ, 2008.

[23] Edwin T. Jaynes, *The well-posed problem*, Foundations of Physics, 3 (1973), pp. 477–493.

[24] A. C. Kak and M. Slaney, *Principles of Computerized Tomographic Imaging*, IEEE Press, New York, 1988.

[25] M. Kempe, M. Larionov, D. Zaslavsky, and A. Z. Genack, *Acousto-optic tomography with multiply scattered light*, Journal of the Optical Society of America A, 14 (1997), pp. 1151–1158.

[26] M. G. Kendall and P. A. P. Moran, *Geometrical Probability*, Charles Griffin & Company Ltd., London, 1963.

[27] P Kuchment, *Mathematics of hybrid imaging. A brief review*, preprint; available at http://arxiv.org/abs/1107.2447, 2011.

[28] P. Kuchment and L. Kunyansky, *Mathematics of thermoacoustic tomography*, European Journal of Applied Mathematics, 19 (2008), pp. 191–224.

[29] P. Kuchment and L. Kunyansky, *Mathematics of thermoacoustic and photoacoustic tomography*, vol. 2 of Handbook of Mathematical Methods in Imaging, Springer, New York, 2010, ch. 19, pp. 817–866.

[30] P. Kuchment and L. Kunyansky, *Synthetic focusing in ultrasound modulated tomography*, Inverse Problems and Imaging, 4 (2010), pp. 665–673.

[31] P. Kuchment and L. Kunyansky, *2D and 3D reconstructions in acousto-electric tomography*, Inverse Problems, 27 (2011), 055013.

[32] P. Kuchment, K. Lancaster, and L. Mogilevskaya, *On local tomography*, Inverse Problems, 11 (1995), pp. 571–589.

[33] P. Kuchment and D. Steinhauer, *Stabilizing inverse problems by internal data*, in preparation, 2011.

[34] L. M. Leemis and K. S. Trivedi, *A comparison of approximate interval estimators for the bernoulli parameter*, The American Statistician, 50 (1996), pp. 63–68.

[35] W. Leutz and G. Maret, *Ultrasonic modulation of multiply scattered light*, Physica B, 204 (1995), pp. 14–19.

[36] S. Lévêque-Fort, *Three-dimensional acousto-optic imaging in biological tissues with parallel signal processing*, Applied Optics, 40 (2001), pp. 1029–1036.

[37] J. Li, *Ultrasound-modulated Optical Tomography for Biomedical Applications*, PhD dissertation, Texas A&M University, 2004.

[38] J. Li and L. V. Wang, *Ultrasound-modulated optical computed tomography of biological tissues*, Applied Physics Letters, 84 (2004), pp. 1597–1599.

[39] X. Li, W. Wang, R. R. Martin, and A. Bowyer, *Using low-discrepancy sequences and the crofton formula to compute surface areas of geometric models*, Computer-Aided Design, 35 (2003), pp. 771–782.

[40] G. D. Mahan, W. E. Engler, J. J. Tiemann, and E. Uzgiris, *Ultrasonic tagging of light: Theory*, Proceedings of the National Academy of Sciences, 95 (1998), pp. 14015–14019.

[41] F. A. Marks, H. W. Tomlinson, and G. W. Brooksby, *Comprehensive approach to breast cancer detection using light: Photon localization by ultrasound modulation and tissue characterization by spectral discrimination*, in Proc SPIE Photon Migration and Imaging in Random Media and Tissues, B. Chance and R.R. Alfano, eds., vol. 1888, 1993, pp. 500–510.

[42] J. Mobley and T. Vo-Dinh, *Optical Properties of Tissue*, Biomedical Photonics Handbook, CRC Press, Boca Raton, 2003, ch. 2.

[43] H. Nam, *Ultrasound Modulated Optical Tomography*, PhD dissertation, Texas A&M University, 2002.

[44] F. Natterer, *The Mathematics of Computerized Tomography*, Society for Industrial and Applied Mathematics, Philadelphia, 2001.

[45] F. Natterer and F. Wübbeling, *Mathematical Methods in Image Reconstruction*, Society for Industrial and Applied Mathematics, Philadelphia, 2001.

[46] G. W. Phillips, *Gamma-ray imaging with Compton cameras*, Nuclear Instruments and Methods in Physics Research Section B: Beam Interactions with Materials and Atoms, 99 (1995), pp. 674–677.

[47] M. H. Protter and H. F. Weinberger, *Maximum principles in differential equations*, Springer, New York, 1984.

[48] G. J. Royle and R. D. Speller, *A flexible geometry Compton camera for industrial gamma ray imaging*, in IEEE Nuclear Science Symposium. Conference Record., vol. 2, 1996, pp. 821–824.

[49] G. J. Royle and R. D. Speller, *Compton scatter imaging of a nuclear industry site*, in IEEE Nuclear Science Symposium, 1997, pp. 365–368.

[50] V. Schonfelder, R. Diehl, G. G. Lichti, H. Steinle, B. N. Swanenburg, A. J. M. Deerenberg, H. Aarts, J. Lockwood, W. Webber, J. Macri, J. Ryan, G. Simpson, B. G. Taylor, K. Bennett, and M. Snelling, *The imaging Compton telescope Comptel on the gamma ray observatory*, IEEE Transactions on Nuclear Science, 31 (1984), pp. 766–770.

[51] M. Singh, *An electronically collimated gamma camera for single photon emission computed tomography. Part I: Theoretical considerations and design criteria*, Medical Physics, 10 (1983), pp. 421–427.

[52] M. Singh and D. Doria, *An electronically collimated gamma camera for single photon emission computed tomography. Part II: Image reconstruction and preliminary experimental measurements*, Medical Physics, 10 (1983), pp. 428–435.

[53] The MathWorks, Inc., *Matlab Statistics Toolbox*, 2011. http://www.mathworks.com/products/statistics.

[54] R. W. Todd, J. M. Nightingale, and D. B. Everett, *A proposed γ camera*, Nature, 251 (1974), pp. 132–134.

[55] T. T. Truong, M. K. Nguyen, and H. Zaidi, *The mathematical foundations of 3D Compton scatter emission imaging*, International Journal of Biomedical Imaging, 2007 (2007).

[56] J. E. Turner, *Atoms, Radiation, and Radiation Protection*, 3rd ed., Wiley-VCH, Weinheim, 2007.

[57] U.S. Department of Transportation, Research and Innovative Technology Administration, Bureau of Transportation Statistics, *America's container ports: Freight hubs that connect our nation to global markets*, 2009. http://www.bts.gov/publications/americas_container_ports/2009.

[58] L. V. Wang, *Mechanisms of ultrasonic modulation of multiply scattered coherent light: A monte carlo model*, Optics Letters, 26 (2001), pp. 1191–1193.

[59] L. V. Wang, *Mechanisms of ultrasonic modulation of multiply scattered coherent light: An analytic model*, Physical Review Letters, 87 (2001), 43903/1-4.

[60] L. V. Wang, *Ultrasound-mediated biophotonic imaging: A review of acousto-optical tomography and photo-acoustic tomography*, Disease Markers, 19 (2004), pp. 123–138.

[61] L. V. Wang, S. L. Jacques, and X. Zhao, *Continuous-wave ultrasonic modulation of scattered laser light to image objects in turbid media*, Optics Letters, 20 (1995), pp. 629–631.

[62] L. V. Wang and S.-I. Wu, *Biomedical Optics. Principles and Imaging*, Wiley-Interscience, Hoboken, NJ, 2007.

[63] E. W. Weisstein, *Sphere point picking*, 2011. From MathWorld–A Wolfram Web Resource, http://mathworld.wolfram.com/SpherePointPicking.html.

VITA

Moritz Allmaras was born in Stuttgart, Germany. He studied Applied Mathematics at Technical University of Munich, where he received a Diplom degree in 2006. In 2006 he obtained a M.S. degree in Mathematics at Georgia Institute of Technology. He subsequently enrolled in the doctoral program in Mathematics at Texas A&M University, where the present dissertation was prepared, and graduated in December 2011. Moritz can be contacted at:

Department of Mathematics

Texas A&M University

3368 TAMU

College Station, TX 77843

USA

E-Mail: moritz@allmaras.de